Nature of Excitons and Their Ligand-Mediated Delocalization in Nickel Dihalide Charge-Transfer Insulators

Connor A. Occhialini,[1,*,†] Yi Tseng,[1,*,‡] Hebatalla Elnaggar,[2] Qian Song,[1] Mark Blei,[3] Seth Ariel Tongay,[3] Valentina Bisogni,[4] Frank M. F. de Groot,[5] Jonathan Pelliciari,[4] and Riccardo Comin[1,§]

[1]*Department of Physics, Massachusetts Institute of Technology, Cambridge, Massachusetts 02139, USA*
[2]*Institut de Minéralogie, de Physique des Matériaux et de Cosmochimi, Sorbonne Université, CNRS UMR 7590, 4 Place Jussieu, 75005 Paris, France*
[3]*Materials Science and Engineering, School for Engineering of Matter, Transport and Energy, Arizona State University, Tempe, Arizona 85287, USA*
[4]*National Synchrotron Light Source II, Brookhaven National Laboratory, Upton, New York 11973, USA*
[5]*Debye Institute for Nanomaterials Science, Utrecht University, 3584 CG Utrecht, Netherlands*

(Received 25 July 2023; revised 23 April 2024; accepted 29 April 2024; published 12 July 2024; corrected 27 August 2024)

The fundamental optical excitations of correlated transition-metal compounds are typically identified with multielectronic transitions localized at the transition-metal site, such as *dd* transitions. In this vein, intense interest has surrounded the appearance of sharp, below-band-gap optical transitions, i.e., excitons, within the magnetic phase of correlated Ni^{2+} van der Waals magnets. The interplay of magnetic and charge-transfer insulating ground states in Ni^{2+} systems raises intriguing questions on the roles of long-range magnetic order and of metal-ligand charge transfer in the exciton nature, which inspired microscopic descriptions beyond typical *dd* excitations. Here we study the impact of charge transfer and magnetic order on the excitation spectrum of the nickel dihalides (NiX_2, $X =$ Cl, Br, and I) using Ni-L_3 edge resonant inelastic x-ray scattering (RIXS). In all compounds, we detect sharp excitations, analogous to the recently reported excitons, and assign them to spin-singlet multiplets of octahedrally coordinated Ni^{2+} stabilized by intra-atomic Hund's exchange. Additionally, we demonstrate that these excitons are dispersive using momentum-resolved RIXS. Our data evidence a ligand-mediated multiplet dispersion, which is tuned by the charge-transfer gap and independent of the presence of long-range magnetic order. This reveals the mechanisms governing nonlocal interactions of on-site *dd* excitations with the surrounding crystal or magnetic structure, in analogy to ground-state superexchange. These measurements thus establish the roles of magnetic order, self-doped ligand holes, and intersite-coupling mechanisms for the properties of *dd* excitations in charge-transfer insulators.

DOI: 10.1103/PhysRevX.14.031007   Subject Areas: Condensed Matter Physics, Magnetism, Strongly Correlated Materials

I. INTRODUCTION

The recent demonstration of magnetic order in correlated transition-metal van der Waals (vdW) materials to the ultrathin limit has led to an increased interest in their excitonic responses and coupling to magnetism. In contrast to uncorrelated, direct band-gap semiconductors exhibiting Wannier-type interband excitons [1], the below-band-gap excitations of strongly correlated transition-metal compounds are typically interpreted in terms of localized transitions between distinct spin or orbital configurations of the transition-metal ions. Also known as *dd* or ligand-field transitions [2], such excitations may be equivalently described as Frenkel-type excitons [3]. Of particular interest is the utility of *dd*-excitation optical responses for measuring and tuning magnetic states, as exemplified by the observation of helical ligand-field luminescence in ferromagnetic Cr trihalides [4,5], the linearly polarized absorption or emission from excitons in the Ni^{2+} vdW magnets NiI_2 [6] and $NiPS_3$ [7–11], and associated photoinduced magnetic properties [12–14]. Clarifying the microscopic origin of such excitonic states, particularly their coupling mechanism to the local spin degree of freedom and long-range magnetism, is essential

[*]Theses authors contributed equally to this work.
[†]caocchia@mit.edu
[‡]tsengy@mit.edu
[§]rcomin@mit.edu

for continued progress toward functional applications and for the optical characterization of magnetic ground states in vdW materials.

Here, we focus on the triangular-lattice nickel dihalide antiferromagnets NiX_2 (X = Cl, Br, I) based on Ni^{2+} ions ($3d^8$) to study their multiplet spectra versus ligand, temperature, and momentum using Ni-L_3 edge resonant inelastic x-ray scattering (RIXS). The ligand-field spectra of Ni^{2+} systems have been the subject of intensive study in classical optical literature [15–21] and more recent studies [6–13,22]. Specifically, several recent investigations report the emergence of sharp excitons below the magnetic transition temperatures of correlated Ni^{2+} vdW magnets [6–11]. These excitons were associated with spin-entangled Zhang-Rice triplet-to-singlet excitations stabilized by long-range magnetic order and magnetic coherence [6,7]. The Zhang-Rice mechanism is motivated by the charge-transfer insulator nature of the electronic ground state in Ni^{2+} systems [23,24]. The electronic states are an admixture between local $3d^8$ and $3d^9\underline{L}$ configurations, where $3d^9\underline{L}$ represents the self-doped ligand-hole electronic configuration [23–25]. From this configuration, analogs to Zhang-Rice states may arise as observed in doped copper oxides [26–28]. Despite this, the reported excitons bear a strong resemblance to optically spin-forbidden multiplet transitions previously revealed by optical spectroscopy [15–21,29,30]. Furthermore, Zhang-Rice states typically refer to an emergent triplet-singlet splitting of the $3d^9\underline{L}$ configuration driven by kinetic exchange [26], much lower in energy than the observed excitations. Based on this dichotomy, the proposed Zhang-Rice mechanism, the role of long-range magnetic order, and the key interactions stabilizing these exciton states require further scrutiny.

The nickel halides provide a platform to assess each of these aspects directly. First, the nickel dihalides are vdW magnets exhibiting distinct ligand-tuned magnetic ground states ranging from C-type antiferromagnetic (AFM) to noncollinear spin structures [6,16,31–33]. Furthermore, they constitute an archetypal series of charge-transfer insulators with systematically tuned Ni-X covalency and charge-transfer gap Δ, as previously revealed through both x-ray photoemission (XPS) and x-ray absorption spectroscopy (XAS) [23,24]. However, the impact that this strongly ligand-tuned Δ has on the ground-state multiplet excitations has not been investigated in detail. As we show in this work, the simultaneous tuning of magnetic order and self-doped ligand holes through the charge-transfer gap establishes their roles in the emergence of the exciton states, and in their fundamental parameters (namely, dispersion, microscopic nature, and temperature effects).

While *dd* excitations are nominally dipole forbidden in optics, RIXS at the transition-metal $L_{3,2}$ edges provides direct spin- and dipole-allowed access to the multiplet spectra of transition-metal compounds [25] without the necessity of coupling to distinct bosonic excitations (e.g., phonons, magnons) or a relaxation of dipole-selection rules through the reduction of point-group symmetry. Such measurements are thus crucial to unravel their microscopic nature, and intrinsic evolution with both temperature and momentum to provide a proper interpretation of their manifestation in optical experiments.

From our RIXS measurements, we observe sharp (nearly resolution-limited) excitonic peaks in all NiX_2 compounds, confirming their universality in Ni^{2+} charge-transfer insulators. The ubiquity of these excitons stems from their microscopic nature, which we assign as spin-singlet ($S = 0$) multiplet (dd) excitations of $^1A_{1g}/^1E_g$ symmetry [34]. These features are characteristic of Ni^{2+} ions in octahedral symmetry, and are broadly consistent with their original identification through optical spectroscopy [15–21,29,30]. Further, the association of these peaks with intraconfigurational multiplets of Ni^{2+} provides a clear rationalization for their characteristically sharp linewidths in both RIXS and optical experiments, determined by their low degeneracy, lack of fine structure, and a quenching of the excited-state coupling to phonons [2,20,21,38,39]. While the energies of these singlet excited states are strongly affected by the ligand and their ionic character, the existence of these excitons does not require particular charge-transfer contributions or long-range magnetic order [25,40]. Using charge-transfer multiplet (CTM) theory, we show that the strong ligand-dependence results from an effective screening of the intra-atomic Hund's exchange interaction (e.g., nephelauxetic effect) [23,25,39,41,42] due to the increasing contribution of self-doped ligand-hole ($3d^9\underline{L}$) states at small Δ. This analysis systematically establishes the primary effects of the metal-ligand hybridization and covalency, and provides a complete description of the multiplet structure in the highly ionic ($NiCl_2$) and strongly covalent (NiI_2) limits.

Using **q**-dependent RIXS, we further uncover a finite momentum dispersion of these spin-forbidden $^1A_{1g}/^1E_g$ multiplets. Such a momentum dependence is fundamentally inaccessible to optical probes ($\mathbf{q} \simeq 0$), yet provides key insight into how the excited singlet states interact with the surrounding crystal and magnetic structure. As the charge-transfer energy is reduced by changing the halogen ligand, the dispersive bandwidth of the singlet excitations increases. Furthermore, the excitons and their dispersive behavior persist far above the magnetic ordering temperatures, demonstrating an exciton delocalization regardless of the presence of long-range magnetism. To explain this, we propose a simple charge-transfer-induced exciton delocalization mechanism determined from the dominant ligand-mediated orbital hopping pathways on the two-dimensional (2D) triangular lattice. This effect can be viewed as a natural consequence of the increased metal-ligand hybridization in a crystalline environment. Our results thus demonstrate that the microscopic interactions stabilizing these excitons are the multielectron interactions at the nickel site, identifying their ubiquity in Ni^{2+} systems. This highlights how their fundamental energies and

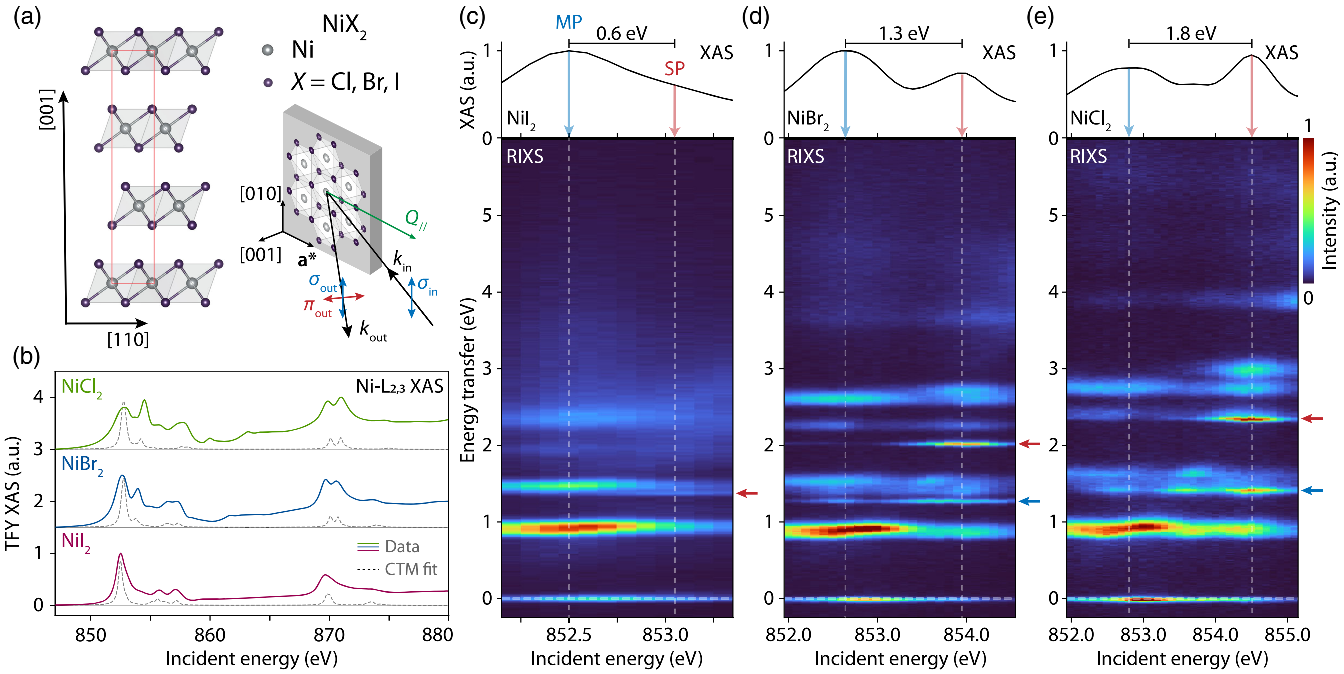

FIG. 1. (a) The layered rhombohedral (space group $R\bar{3}m$) structure of NiX_2 dihalide compounds, highlighting the triangular lattice of magnetic Ni^{2+} ions and the RIXS scattering geometry at grazing incidence (see text). (b) Ligand-dependent Ni-L_3/L_2-edge XAS spectra at $T = 40$ K. Corresponding XAS fits from charge-transfer multiplet calculations are the dashed gray lines (see text). (c)–(e) Incident-energy-dependent RIXS maps for each compound across the main and side peaks at the Ni-L_3 edge (bottom) with the corresponding total fluorescence yield (TFY) XAS spectra (top). The XAS spectra indicate the main peak and side peak (MP, SP) resonances with blue and red arrows, respectively, along with the MP-SP incident-energy splitting for each compound. Red and blue arrows on the right axis of each RIXS map indicate the $^1A_{1g} - {}^1E_g$ spin-singlet multiplets resonant at the XAS SP.

degree of delocalization may be tuned through the charge-transfer gap.

Our paper is organized as follows: (i) We present the experimental Ni-L_3 edge RIXS and XAS data versus ligand in the nickel dihalide series in Sec. II A. (ii) We model the spectra with NiX_6 cluster calculations using charge-transfer multiplet theory to establish the microscopic origin of each excitation, and determine the role of the self-doped ligand holes in the ground and excited states in Sec. II B. (iii) We present momentum and temperature dependence of the spin-forbidden $^1A_{1g}/{}^1E_g$ multiplets in comparison with spin-excitation dispersions in Sec. II C, and (iv) we propose a microscopic model for the multiplet dispersion in Sec. II D. Finally, we discuss the implications of these results in Sec. III and conclusions in Sec. IV.

II. EXPERIMENTAL RESULTS

We perform XAS and RIXS measurements on high-quality single crystals of NiX_2 compounds grown by chemical vapor transport (see Appendix A). The RIXS and XAS data are acquired at the 2-ID SIX beamline of the National Synchrotron Light Source II, Brookhaven National Laboratory [43]. RIXS measurements are performed with an energy resolution of $\Delta E = 31$ meV at the Ni-L_3 edge, and XAS is recorded in total fluorescence yield (TFY). The samples are aligned with the $\mathbf{a}^*$ reciprocal lattice direction aligned in the scattering plane [Fig. 1(a)], with grazing incidence geometry, σ incident polarization, and $T = 40$ K unless otherwise specified. The temperature is chosen to be below the magnetic phase transitions for each compound.

A. Evolution of RIXS and XAS spectra versus ligand

We begin by discussing the evolution of the Ni-L_3 edge RIXS and XAS spectra versus ligand (X) for NiX_2. Figure 1(b) shows XAS spectra across the Ni-L_3/L_2 edges for each compound. At the L_3 edge, a clear double-peaked structure is observed for all compounds corresponding to a “main” peak (MP) around 852.7 eV, followed at higher energy by a side peak (SP) at 854.5, 854.0, and 853.1 eV for $NiCl_2$, $NiBr_2$, and NiI_2, respectively [see Figs. 1(c)–1(e), top]. We note the pronounced self-absorption effect in the TFY XAS spectra [24,44–46], leading to suppression of main L_3-edge intensity (see Supplemental Material [47]). The energy separating the MP and SP increases with the ionic character of the compound. The latter is directly linked to higher charge-transfer gaps Δ, as discussed below.

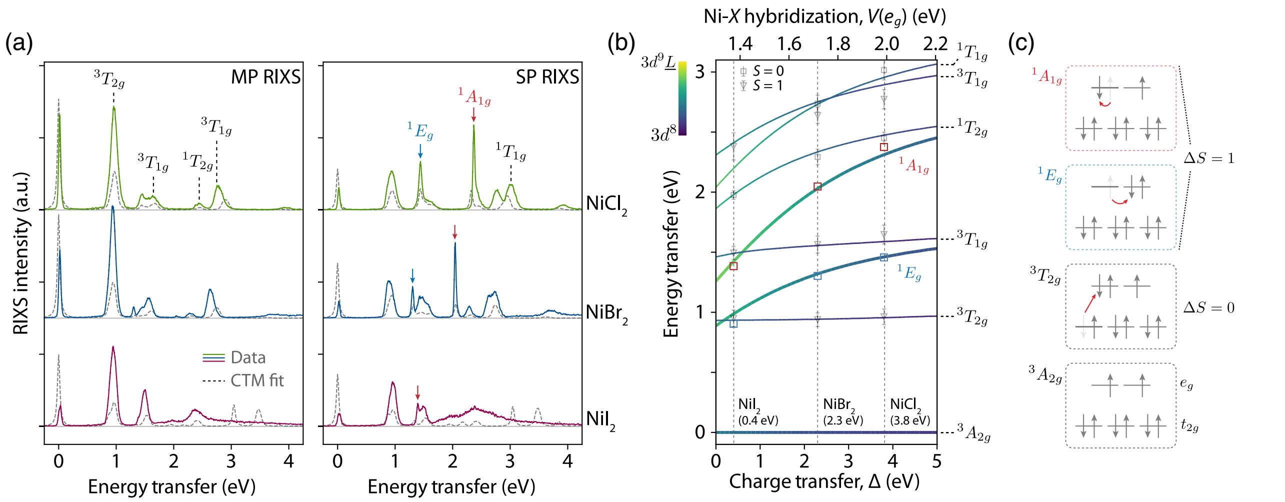

FIG. 2. (a) Ligand-dependent RIXS spectra at the MP (left) and SP (right) resonances. Intensity for each spectrum has been normalized by the total inelastic signal ($0.5 \rightarrow 5.0$ eV). The peaks are labeled with their corresponding multiplet term symbol in O_h symmetry (see text). The sharp spin-singlet excitations (^1E_g and $^1A_{1g}$) are indicated for each compound with blue and red arrows, respectively. Corresponding charge-transfer multiplet (CTM) calculations are shown as dashed gray lines overlaid with each experimental spectrum. The sharp features in the CTM calculations for NiI_2 above 3 eV are charge-transfer transitions, which are broad and overlap with fluorescent background in experiment (thus, not well resolved). The lower-energy $3d^8$ multiplets in all NiX_2 samples are sharp and well captured by CTM calculations. (b) Energy-level diagram calculated from the CTM model as a function of the charge-transfer gap Δ and Ni-X hybridization $V(e_g)$ in O_h symmetry (spin-orbit coupling excluded for simplicity). The $^1A_{1g}$ and ^1E_g term energies are highlighted with thick lines, and all calculated excitations are colored based on the $3d^8/3d^9\underline{L}$ character, as indicated by the color bar. Experimental energies for the $^1A_{1g}/^1E_g$ peaks are shown as red and blue data points, respectively, with other experimental multiplets indicated with triangles and squares for triplet and singlet terms, respectively. Optimal fit values of Δ for each compound are indicated with vertical dashed lines. An approximate relation between the metal-ligand hybridization $V(e_g)$ (top axis) and the charge-transfer energy Δ (bottom axis) for the NiX_2 series is determined to be $V(e_g) = 0.181\Delta + 1.301$ from independent CTM model fits to all compounds, as discussed in Appendices A and B. (c) Schematic representation of the low-energy $\Delta S = 0/\Delta S = 1$ $3d^8$ multiplet terms in O_h symmetry.

Additionally, several broader peaks are observed at higher energies ($E_i \simeq 855$–860 eV) and associated with charge-transfer satellites [24,25,42]. An overall similar qualitative behavior is observed at the L_2 edge.

We subsequently measure RIXS spectra versus incident energy across the MP and SP resonances at the Ni-L_3 edge for each compound [Figs. 1(c)–1(e)]. For Ni^{2+} in octahedral (O_h) symmetry, the ground-state electronic configuration is $^3A_{2g}$ with $t_{2g}^6 e_g^2$ orbital occupation and $S = 1$ arrangement of the half-filled e_g states [2,48]. Around $\Delta E = 950$ meV energy transfer, we identify a predominant Raman-like excitation which is nearly independent of the ligand. This excitation is connected to the fundamental $t_{2g} \rightarrow e_g$ spin-preserving ($\Delta S = 0$) crystal-field excitation ($^3T_{2g}$), suggesting a similar O_h crystal-field energy scale ($10Dq$) across the series [40]. The independence of this energy scale with a ligand can be rationalized by the balance of charge-transfer and metal-ligand hybridization contributions, both of which affect the covalent crystal-field splitting as captured by our CTM calculations and discussed below [26,49,50]. At higher energies ($\Delta E = 1$–3 eV), rich excitation profiles are resolved with a strong ligand dependence. These peaks are linked to the multiplet structure of Ni^{2+} in O_h symmetry [2,25,40,51]. We highlight the uniquely sharp excitations around 1.38, 2.04, and 2.37 eV in I, Br, and Cl [red arrows, Figs. 1(c)–1(e)], respectively. These peaks are nearly resolution-limited and resonant near the SP. Additional sharp excitations at the SP near $\Delta E = 1.3$ and 1.45 eV in Br and Cl (blue arrows), respectively, are also observed.

The ligand-dependent RIXS spectra at the MP and SP resonances are summarized in Fig. 2(a). The individual dd transitions are assigned with term symbols in O_h symmetry for $NiCl_2$ (top) based on our CTM calculations. Specifically, the higher- and lower-energy sharp peaks resonant at SP are ascribed to the spin flip $\Delta S = 1$ and $^1A_{1g}/^1E_g$ multiplet terms, respectively [40,51], which both preserve the ground-state $t_{2g}^6 e_g^2$ orbital configuration. These spin-singlet multiplets are equivalent to the previously identified excitons in the optical regime, appearing at the same energies [6,7,15–17,29,30]. The salient features of the ligand dependence can be summarized by (i) a reduction of the MP-SP splitting in XAS, (ii) a reduction of multiplet energies that is most pronounced in the spin-singlet $^1A_{1g}$ and ^1E_g excitations, and (iii) the resonant behavior of the $\Delta S = 1$ excitations at the ligand-dependent SP resonance.

TABLE I. Ligand dependence of Δ and $V(e_g)$ from CTM calculations. Coulomb interactions are fixed to atomic values, and the ionic contribution to $10Dq = 0.55$ eV is fixed for all ligands. The on-site Coulomb repulsions are fixed to $U_{dd} = 5.0$ eV and $U_{pd} = 7.0$ eV from photoemission experiments [23]. Also shown is the phenomenological, effective ground-state nephelauxetic reduction (β_{eff}) and intra-atomic Hund's exchange (J_H^{eff}) determined from corresponding ionic calculations in Appendix B.

Ligand (X)	Δ (eV)	$V(e_g)$ (eV)	β_{eff}	J_H^{eff} (eV)
Cl	3.80	1.99	0.75	0.850
Br	2.30	1.72	0.64	0.722
I	0.40	1.37	0.44	0.496

B. NiX_6 cluster calculations

We next aim to quantitatively describe these ligand-dependent spectroscopic features and provide a robust assignment of the electronic ground states and excitations. To do so, we employ CTM calculations as implemented in QUANTY [52–54]. The model reduces to a multielectronic calculation of a single NiX_6 cluster with O_h symmetry, accounting for the Ni-$3d$ orbitals and the corresponding symmetrized ligand X-np molecular orbitals [24,25,52] (see Appendix A). We restrict the present analysis to O_h symmetry, while potential effects of the trigonal distortion are discussed in the Supplemental Material [47]. Figure 2(b) shows the evolution of low-energy multiplets for the $3d^8 + 3d^9\underline{L} + 3d^{10}\underline{L}^2$ configurations as a function of Δ. The evolution of the ${}^1A_{1g}$ and ${}^1E_g$ excited states as a function of the ligand charge transfer are highlighted with thick lines [Fig. 2(b)]. These excitations correspond to a nearly pure spin flip $\Delta S = 1$ within the $|e_g\rangle$ manifold without transfer of orbital weight between the t_{2g}-e_g states. Thus, they are stabilized from the ${}^3A_{2g}$ ground state by the intra-atomic Hund's exchange [2] (see also Ref. [55]). Their preservation of the $t_{2g}^6 e_g^2$ ground-state orbital configuration, in conjunction with their low degeneracy, naturally accounts for their characteristically sharper linewidths compared to the other interconfigurational multiplets [15,35,36,39].

We identify the optimal parameters for each compound based on a minimal parameter fitting while keeping the Coulomb interactions at the nickel site fixed (for a detailed description of the model and parameters, see Appendices A and B). The optimized ligand-dependent CTM parameters Δ and the metal-ligand hybridization $V(e_g)$ are summarized in Table I and indicated as vertical dashed lines in Fig. 2(b), with the experimental values of multiplet energies overlaid. The refined parameters are broadly consistent with previous reports from XPS and XAS [23,24], while our calculations are further restricted by the multiplet spectra, which more accurately reflect the ground-state Hamiltonian. The simulated XAS and RIXS spectra determined from these parameters are shown as gray lines on top of the experimental data in Figs. 1(c) and 2(a). They reveal good agreement with all salient features of the ligand dependence, including the peak energies [Fig. 2(b)], their resonance behavior and relative intensities [Fig. 2(a)], as well as the MP-SP and charge-transfer satellite structures in the XAS [Fig. 1(b); for calculated RIXS maps to compare to experiments in Figs. 1(c)–1(e), see Appendix B].

A consequence of reduced Δ is a larger mixing of the $3d^9\underline{L}$ configuration into the ground- and excited-state $3d^8$ multiplets [6,7,24,25,40,42,56,57]. The energy-level diagram in Fig. 2(b) shows the evolution between $3d^8$ and $3d^9\underline{L}$ character resolved to each excitation. The ligand-hole character is excitation dependent, with higher-energy excitations within a given orbital configuration (e.g., $t_{2g}^6 e_g^2$ vs $t_{2g}^5 e_g^3$) displaying larger ligand character at a given Δ, with the $|3d^9\underline{L}\rangle$ weight roughly commensurate to the energetic renormalization of each excitation. A similar situation determines the energy-dependent ligand-hole character and MP-SP reduction in the XAS intermediate states. Besides this energetic renormalization, all excitations remain direct analogs of the corresponding $3d^8$ multiplets as they stem only from the electronic configuration and point-group symmetry (see Appendix B).

We conclude that the dominant role of ligand-hole states at the level of a single NiX_6 cluster is a renormalization of the intra-atomic Coulomb interactions in both the initial and final RIXS states. This renormalization results from the delocalization of electronic density onto the ligand states (e.g., the nephelauxetic effect [23,25,39,41,42]). This screening effect captures the evolution of the sharp singlet excitations, their resonance behavior, and the MP-SP evolution, which can be mapped to properties of Ni^{2+} ions in O_h symmetry without invoking emergent properties from the $3d^9\underline{L}$ configuration. From this assessment, the relevance of an underlying Zhang-Rice (e.g., kinetic exchange) mechanism for these excitations can be ruled out [11]. These excitations are instead determined by the Hund's coupling at the nickel site. Thus, the sharp ${}^1A_{1g}$ and ${}^1E_g$ peaks are best described as Ni^{2+} dd excitations arising from multielectronic interactions of a $3d^8$ electronic configuration in O_h crystal field. One may therefore expect such excitations to be ubiquitous in isoelectronic systems close to the ionic limit [6,7,15,25,39–41,58]. These conclusions are directly supported by calculations restricted to the purely ionic limit with $3d^8$ configuration and excluding charge-transfer processes summarized in Appendix B. Indeed, the effect of ligand holes on the multiplet excitations can be captured by an effective nephelauxetic effect (β_{eff}), as summarized in Table I.

C. Exciton dispersion and relation to magnetism

Having established the presence and properties of the exciton peaks in NiX_2 as a function of the ligand, as well

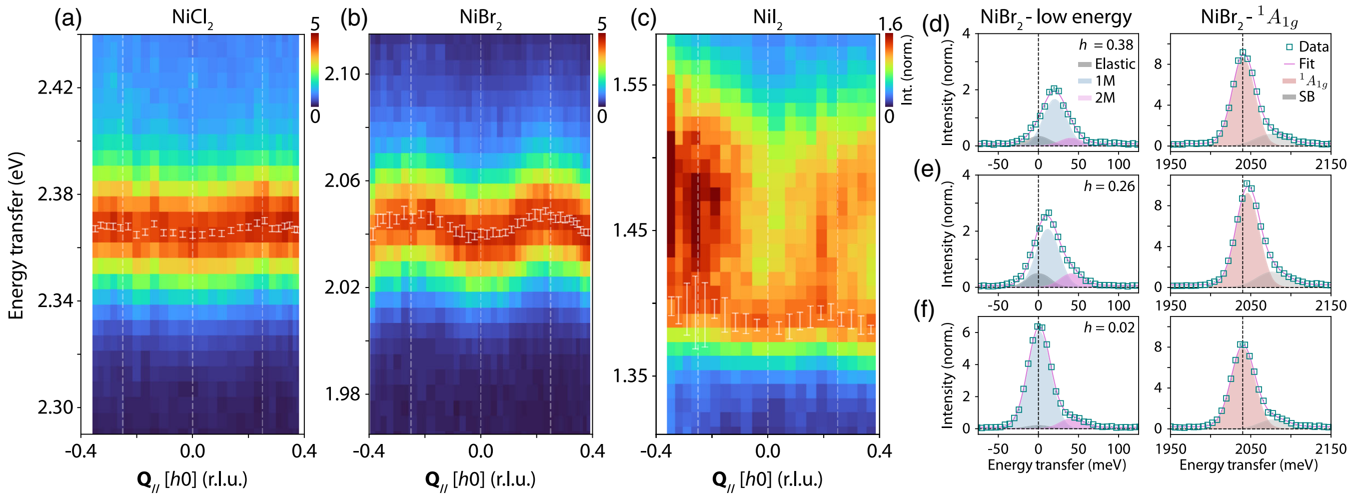

FIG. 3. Momentum dependence of the $^1A_{1g}$ peak as a function of the ligand at $T = 40$ K in panels (a), (b), and (c) for Cl, Br, and I along the ΓM direction, respectively. Momentum is reported as $\mathbf{Q}_\parallel = [h0]$ with h expressed in reciprocal lattice units (r.l.u.). Color maps are normalized to the integrated intensity of the displayed region in (a) and (b) and to the region 1.35–1.42 eV in (c). Fitted points for the $^1A_{1g}$ peak are shown as overlaid white data points with error bars determined as standard errors from the fits. Panels (d)–(f) are example raw data along ΓM with $h = 0.38$, 0.26, and 0.02, respectively, for $NiBr_2$ both in the low-energy transfer (left) and $^1A_{1g}$ spectral regions (right), highlighting fits to the elastic (gray), single- and two-magnon (1M and 2M, blue and purple, respectively) contributions, and the $^1A_{1g}$ peak (red) and its SB (gray), with overall fit depicted in purple. Statistical error bars are indicated, which are smaller than the data points.

as their hybridized Ni and halogen nature, we now investigate their dependence on momentum and temperature to assess their delocalization beyond pure on-site dd excitations [59–61] and their connection to the magnetic order.

We first report the dispersion of the $^1A_{1g}$ excitation for each ligand in Figs. 3(a)–3(c), measured at $T = 40$ K with momentum transfer along the $\mathbf{a}^*$ direction ([h0] in r.l.u.) and with incident energy tuned to the SP resonance (Figs. 1 and 2). We resolve an electronic dispersion with bandwidth $\delta E \simeq 3.4 \pm 1.2$ meV in $NiCl_2$, $\simeq 8.2 \pm 1.3$ meV in $NiBr_2$, and $\simeq 9.6 \pm 3.0$ meV in NiI_2. Representative fits for spectra at selected momentum-transfer points for $NiBr_2$ are displayed in Figs. 3(d)–3(f) showing both the low-energy and $^1A_{1g}$ spectral regions. Both spectral regions are from the same spectra at a given $\mathbf{Q}_\parallel$ recorded at the SP resonance where single- and two-magnon contributions are observed [40,51,62,63]. The spectra are relatively aligned using $\Delta S = 0$ multiplet excitations, which assumes these excitations are nondispersive. This assumption can be justified by their high multiplicity, significant phonon broadening, and the relatively low contribution of the $3d^9\underline{L}$ configuration, leading to the same spectral center of mass (i.e., lack of apparent dispersion). The corresponding analysis is discussed further in the Supplemental Material alongside additional discussion of polarization cross-section and multiplet fine-structure effects [47]. Momentum dependence for the ^1E_g excitation is also resolved in $NiCl_2$ and $NiBr_2$ [47].

To elucidate the microscopic origin of the exciton dispersion and its reciprocal-space structure in more detail, we perform momentum-dependent RIXS measurements across the magnetic phase transition and along different high-symmetry directions in reciprocal space, with a focus on $NiBr_2$. In Figs. 4(a) and 4(b), we plot the fitted energy dispersion for the low-energy magnon and $^1A_{1g}$ mode in $NiBr_2$, with comparison along the ΓM ([h0] r.l.u.) and ΓK directions ([hh] r.l.u.). The magnon and $^1A_{1g}$ exciton dispersion along ΓM are further compared at 40 and 70 K representing the layered AFM and paramagnetic phase of $NiBr_2$, respectively [15,16,32]. From these data, we infer marginal differences in the $^1A_{1g}$ dispersion across the magnetic phase transition [Fig. 4(b)], with the primary temperature effect being an overall broadened linewidth with increasing temperature (as discussed below). This implies that the exciton dispersion is present regardless of long-range magnetic order, and therefore is likely not mediated by it.

The magnon dispersions are compared with linear-spin-wave (LSW) calculations [Fig. 4(a)] based on inelastic neutron scattering in the layered AFM phase [32], showing good quantitative agreement (for similar comparisons in $NiCl_2$ [31], see Supplemental Material [47]). Importantly, the magnon and the $^1A_{1g}$ peaks have qualitatively distinct dispersions along ΓK and ΓM. From Figs. 3(a)–3(c), we also note the qualitatively similar functional form of the $^1A_{1g}$ dispersion across all compounds, which is independent of the disparate magnetic structures or spin excitation

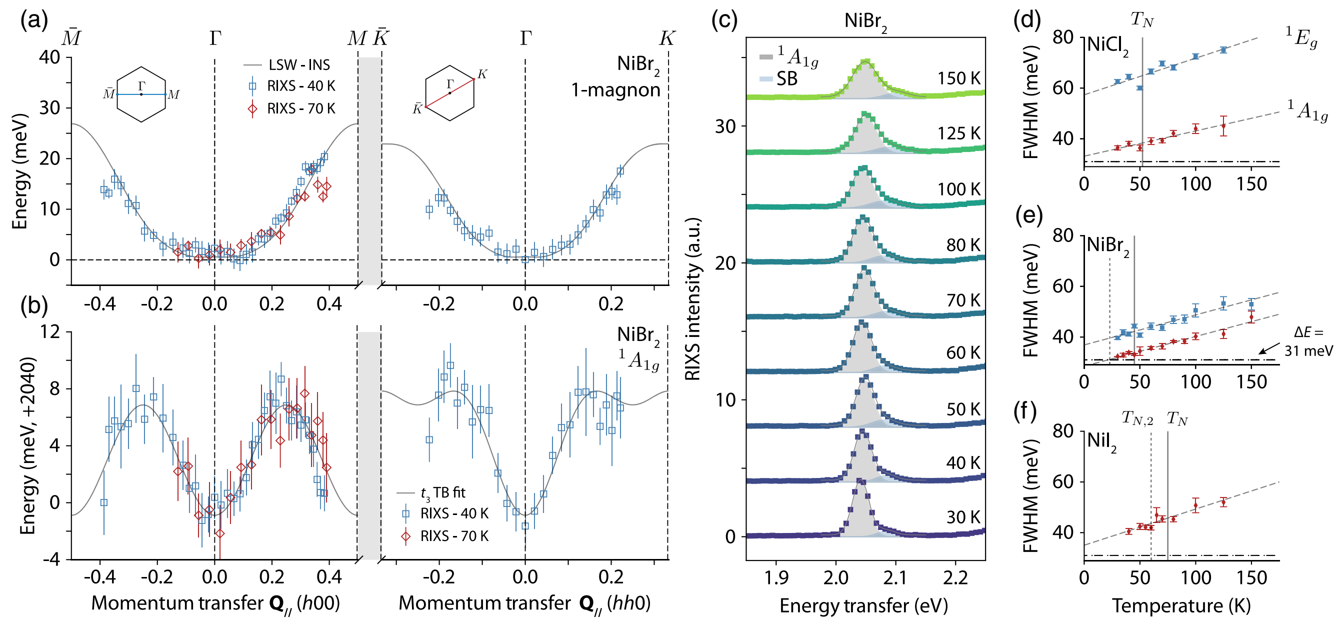

FIG. 4. Momentum dependence of the single magnon (a) and the $^1A_{1g}$ excitation (b) in $NiBr_2$ along the ΓM (left) and ΓK (right) momentum-space cuts. Blue squares $T = 40$ K and red diamonds $T = 70$ K. Experimental single-magnon energies are compared to linear spin wave (LSW) theory, accounting for intralayer exchange up to third nearest neighbor (J_3) using experimentally determined parameters from Ref. [32]. The $^1A_{1g}$ data are fit along both ΓM and ΓK with a tight-binding (TB) model considering only third-nearest-neighbor hopping (t_3). The LSW and TB curves are shown as solid gray lines in (a) and (b), respectively. (c) Representative temperature dependence of the $^1A_{1g}$ excitation in $NiBr_2$ highlighting the temperature-dependent linewidth. Gaussian fits to the $^1A_{1g}$ and its side band (SB) (see text) are the filled gray and blue curves, respectively. Temperature-dependent linewidth of the $^1A_{1g}$ (red) and ^1E_g (blue) peaks for (d) $NiCl_2$, (e) $NiBr_2$, and (f) NiI_2. Linear fits (dashed lines) highlight a linear broadening of each peak with increasing temperature. Horizontal dashed lines denote the experimental resolution ($\Delta E = 31$ meV) for all measurements. Vertical solid lines indicate the C-type AFM transition temperature $T_N \simeq 52$, 45, and 75 K for Cl, Br, and I, respectively, and dashed lines indicate the noncollinear magnetic phases $T_{N,2} \simeq 22$ and 60 K for Br and I, respectively [16,31,64].

dispersions (see also Supplemental Material Fig. S9 [47]). These aspects support our assignment of a genuine dispersion of the $^1A_{1g}$ excitations. To quantify this, we construct a minimal tight-binding (TB) model based on isotropic hopping parameters t_n up to $n = 3$ nearest neighbor (NN) [3,35,65,66]. We find that the $^1A_{1g}$ dispersion is well described by considering only the third-NN contribution, with the single-parameter (t_3) fit for $NiBr_2$ reported in Fig. 4(b). We note that the spin excitations persist above the long-range-ordering temperatures [Fig. 4(a)], suggesting the presence of short-range magnetic correlations persisting to high temperatures [67–69]. An effect of these short-range magnetic correlations for determining the spin-singlet multiplet dispersion cannot be ruled out directly, although we will argue for a more natural mechanism as evidenced by the ligand dependence (discussed below).

To further underscore the independence of the $\Delta S = 1$ multiplets from the magnetic order, we measure the temperature dependence at fixed momentum transfer across the magnetic phase transitions in each compound as reported in Figs. 4(c)–4(f). A monotonic linewidth broadening is revealed for both the $^1A_{1g}$ and ^1E_g modes without any significant change of spectral profiles across the magnetic phase transition temperatures for each NiX_2 compound [Figs. 4(d)–4(f)]. For $NiBr_2$ [Fig. 4(c)], additional spectral weight at higher energies (30–40 meV) above the $^1A_{1g}$ peak is apparent, which is attributed to two-phonon sidebands, consistent with previous optical experiments [15,16,18–21]. Importantly, the linewidth and intensity of the singlet peaks are independent of the magnetic phase. In addition, we do not observe any clear correlation between the thermal broadening slope or extrapolated zero-temperature linewidth with either the magnetic transition temperatures (as may be expected for magnetic coherence) or with the $|3d^9\underline{L}\rangle$ character of the excitations [Figs. 4(d)–4(f)]. Instead, we attribute the thermally activated broadening to a Franck-Condon phonon-coupling effect [15,48,70].

Before moving on, we summarize the experimental observations and what they imply regarding the role of magnetism for these multiplet states. From the charge-transfer multiplet calculations, we identify the microscopic origin of the excitations as the $^1A_{1g}/^1E_g$ exciton states related to the local spin degree of freedom via Hund's exchange. From the temperature-dependent RIXS at fixed

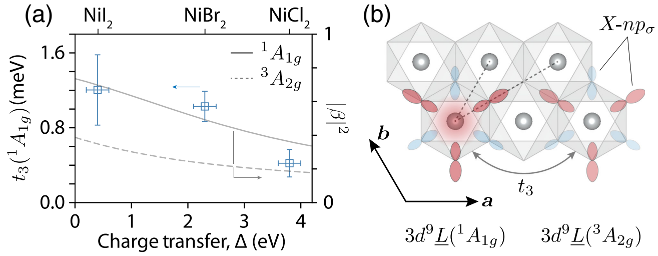

FIG. 5. (a) Ligand dependence of the t_3 TB parameter from fits to the $\mathbf{a}^*$ dispersion data presented in Figs. 3(a)–3(c) (left axis, blue), along with the $3d^9\underline{L}$ character ($|\beta|^2$) of the excited-state $^1A_{1g}$ (solid) and the ground-state $^3A_{2g}$ (dashed) multiplets extracted from the CTM calculations in Fig. 2(b) (right axis). (b) Schematic of the hopping pathways in the triangular-lattice plane (t_1-t_3) and the proposed third-nearest-neighbor hopping mechanism between the $3d^9\underline{L}(^1A_{1g})$ excited state and $3d^9\underline{L}(^3A_{2g})$ ground state mediated by ligand p-p σ-bonding molecular orbitals.

$\mathbf{q}$, we observe that the spectral signatures of these localized dd excitations (linewidth, energy) are independent of long-range magnetic order. Separately, we observe a finite dispersion of the $^1A_{1g}/^1E_g$ excitations for all ligands, independent of the disparate spin structures and qualitatively distinct from the spin excitation dispersions across the NiX_2 series. Overall, the experimental evidence consistently suggests that there is no direct effect of long-range magnetic order on the bare multiplet states, or in their dispersive character. This leads us to consider a mechanism of exciton delocalization that does not invoke magnetism, but instead directly originates from an increased contribution of the self-doped ligand holes with reduced Δ.

D. Origin of exciton dispersion

To examine the origin of the finite $^1A_{1g}$ dispersion, we consider the ligand dependence of the dispersive bandwidth (t_3). This is displayed in Fig. 5(a), extracted from the $\mathbf{a}^*$ dispersion in Figs. 3(a)–3(c), revealing an increase of the bandwidth with decreasing Δ. The ligand-dependent bandwidth follows the trend of the projected $3d^9\underline{L}$ character of the $^1A_{1g}$ state [$|\beta^2|$ in Fig. 5(a)], implicating a ligand-mediated delocalization mechanism. The ligand origin of this effect is also suggested by the dominance of third-NN interactions evidenced by the functional form of the dispersion, suggesting long-range interactions beyond direct $d \rightarrow d$ overlap. We interpret these features in analogy to the evolution of magnetic exchange interactions throughout the dihalide series, which have been analyzed in detail in the literature [31–33,64,71]. The spin exchange is dominated by superexchange [56,72], with moderate ferromagnetic J_1, negligible J_2, and antiferromagnetic J_3 parameters restricted to the 2D triangular-lattice plane where J_n is the nth Ni-Ni neighbor exchange [71]. While J_1 exhibits moderate stoichiometric dependence, J_3 is strongly ligand dependent and is responsible for the difference in magnetic ground states across the series, including the noncollinear magnetic states in $X =$ Br, I [32,33,71,73]. Specifically, J_3 is mediated by superexchange pathways involving ligand X-np molecular orbitals with large σ-type overlap [56], as depicted in Fig. 5(b).

From this picture, a dominance of the t_3 TB component in the $^1A_{1g}$ dispersion can be explained by the stronger $pp\sigma$ ligand-ligand transfer integrals between third-NN $3d^9\underline{L}$ e_g-symmetry molecular orbitals, in conjunction with the lowering of the charge-transfer gap which mediates pd electron transfer and increases the self-doped $3d^9\underline{L}$ character [23,25,56,57]. While superexchange occurs between Ni atoms in the $^3A_{2g}$ ground state, the dispersion we observe originates from interactions between an excited $^1A_{1g}$ impurity and a surrounding bath of $^3A_{2g}$ [35,36] [Fig. 5(b)]. The enhancement of $3d^9\underline{L}$ character upon excitation of the effective $^1A_{1g}$ defect compared to the $^3A_{2g}$ ground state [Fig. 5(a)] could contribute to these observations due to selective enhancement of the excited-state third-NN interactions, which are more sensitive to the ligand-hole contribution compared to nearest-neighbor interactions [56].

These considerations are not unique to the $^1A_{1g}$ state, as a finite dispersion was also resolved for the ^1E_g state (see Supplemental Material [47]). For ^1E_g, the dispersion is weaker and with opposite sign relative to the $^1A_{1g}$ but of a similar qualitative (sinusoidal) form with increased bandwidth from $NiCl_2$ to $NiBr_2$ (see Supplemental Material Fig. S9 [47]). This suggests the sensitivity of the proposed hopping processes to the relative spin-orbital character of the excited and ground states, again analogous to Pauli-restricted virtual hopping processes leading to superexchange [26,35,56]. We note that since the ^1E_g and $^1A_{1g}$ states are $S = 0$ (nonmagnetic), this should be interpreted as a multiplet-dependent effective transfer integral that is independent of the relative alignment of the surrounding $^3A_{2g}$ ground-state spins—that is, independent of the long-range magnetic order. This scenario is consistent with the insensitivity of the spin-singlet multiplets and their dispersion to the magnetic transitions (Fig. 4).

While the hopping is independent of magnetic order, the final state with an exchanged exciton and ground-state spin may couple to magnetic excitations, as claimed in iridates and cuprates [61,74–77]. We do not observe any direct experimental evidence for the resulting magnon renormalization of the exciton dispersion, but this could be reconciled with the persistence of both short-range magnetic correlations and $^1A_{1g}$ exciton dispersion above T_N [Fig. 4(a)]. From this perspective, we note that the standard model mapping the problem of exciton propagation to that of a single-hole hopping on an AFM background is not directly applicable to the case of NiX_2, due to the different 2D magnetic order. Thus, further theoretical investigations are required to clarify the essence of this exciton delocalization and its coupling to electronic and magnetic degrees of freedom through, e.g., dynamical mean field theory [78]. Nonetheless, the mode-resolved and Δ-dependent dispersive behavior presented here provides key constraints for reaching a consistent microscopic description of excitonic dispersion in charge-transfer insulators.

III. DISCUSSION

Our results reveal the momentum dependence of spin-singlet *dd* excitations in NiX_2 compounds, and we propose a ligand-mediated delocalization mechanism analogous to superexchange. Specifically, the microscopic interactions that give rise to the $^1A_{1g}/^1E_g$ excitations are rooted in the $3d^8$ electronic configuration in octahedral symmetry, i.e., *dd* excitations. Meanwhile, increasing metal-ligand charge transfer induces two intertwined, but distinct, effects. First, it renormalizes the intra-atomic Coulomb interactions at the Ni site and induces a corresponding reduction of the fundamental multiplet energies (Figs. 1 and 2). Second, the excitations simultaneously develop an increasingly delocalized and propagating nature, independent of the magnetic phase (Figs. 3–5). These conclusions provide a self-consistent and comprehensive picture of the influence of metal-ligand charge transfer on the properties of multiplet excitations in charge-transfer insulators.

The importance of measuring the exciton dispersion for unraveling its underlying nature has been stressed in several different contexts, including the alkali halides [79], spin-state excitations in cobaltites [78], fractionalized orbitons in low-dimensional cuprates [59–61,74], spin-orbit excitons in iridates [75–77], and molecular excitons [65,80–82]. The multiplet dispersion reported here is distinct from the case of orbitons in cuprate spin chains [59,60], which is an emergent effect from low dimensionality. Further, our observations provide a uniquely simple example of a dispersive, purely multi-electronic excitation beyond the cases of iridates and cobaltites [75,76,78], while further establishing how this dispersive behavior evolves over a range of electronic energy scales. In particular, our work highlights the key role of the ligand states and charge-transfer processes in mediating the exciton dispersion. This was also recently suggested in 2D cuprates, where explicit consideration of the ligands is critical to achieve the correct qualitative and quantitative form of the dispersion [61].

In a different context, the dispersion of these spin-flip multiplets is also important for the microscopic description of exciton-magnon sidebands in optics [15,16,19–21,35–37,83]. The momentum dependence of the exciton state contributes to the optical sideband structure and also determines the mechanisms of intersite exciton-magnon coupling [3,35,36], which are of strong relevance for interpreting photoinduced magnetic responses in transition-metal and vdW materials [10,12,14,35,36,84–89]. Our results provide direct evidence of the exciton dispersion. This observation uniquely resolves the measured *dd* excitons' character, which clarifies ongoing debates regarding magnetoexciton coupling in vdW magnets.

Furthermore, our temperature-dependent RIXS results (Fig. 4) provide important context for the observation of these spin-flip *dd* excitations in the optical regime [6,7,11,16–18,29]. These multiplet transitions are optically dipole and spin forbidden, and therefore their observation by optical probes is sensitive to the lowering of symmetry across (magnetic) phase transitions and are typically inferred from optical sidebands of bosonic origin (e.g., phonon, magnon [15,18–21]). The complexity of such a rich sideband structure, as well as the large energetic renormalization of the spin-forbidden peaks as a function of the charge-transfer gap, has precluded consistent peak assignments and interpretations in the optical literature which we conclusively resolve. One consequence of the coupling to bosons is that the optical response of these exciton sidebands can be sensitive to the coherence of the magnon excitations [19–21]. The proposed effects of magnetic coherence are then likely attributed to the (magnetic) $^3A_{2g}$ ground state rather than the (nonmagnetic) $^1A_{1g}/^1E_g$ excited states. Conversely, the fundamental spin-flip multiplets, generally a high cross section and direct RIXS process at the transition-metal *L* edges, are well defined and independent of magnetic order with line shape limited only by a temperature-dependent Franck-Condon phonon broadening [Figs. 4(c)–4(f)]. Current experiments do not provide conclusive evidence for a dependence of the optical spectral weight of the NiX_2 multiplets on the magnetic order parameter (except $NiBr_2$ [16], which may relate to magnon sidebands, yet phonon broadening preceding at lower temperature could not be ruled out [20]). Nonetheless, our work establishes that the effects of magnetic order in optical experiments, if any, are related to details of the optical cross section and are not relevant to the fundamental properties of the multiplets themselves.

Finally, we demonstrate several key design principles for tuning the exciton properties. The sharp (nearly resolution-limited) linewidths of the identified $^1A_{1g}/^1E_g$ multiplets are rationalized by their intraconfigurational nature, which minimizes the excited-state lattice coupling within a Franck-Condon-type picture. This association provides a natural explanation of the qualitatively different linewidths compared to the other (interconfigurational) multiplets of NiX_2, as well as with the ligand-field transitions reported in other compounds (e.g., $CrI_3/CrBr_3$ [4,5] and $FePS_3/MnPS_3$ [87]). However, we note that only the isolated $^1A_{1g}$ peak in $NiBr_2$ has a resolution-limited behavior at the lowest measured temperature ($T = 30$ K). This contrasts with the $^1A_{1g}$ excitations of $NiCl_2$ and NiI_2 which are broader than the experimental resolution and are partially or fully overlapped with other multiplets. We hypothesize that a spin-orbit-coupling-induced hybridization of closely lying multiplets with distinct orbital configurations (e.g., $t_{2g}^6 e_g^2$ and $t_{2g}^5 e_g^3$) may be an important aspect limiting the intrinsic (low-T) linewidths. Furthermore, to make these modes optically bright with large oscillator strength, details of multiplet-level sequencing (particularly the lowest excited state) and relative energetic proximity of different multiplet terms are known to be essential through, e.g., intersystem crossing and intensity borrowing mechanisms [39]. These mechanisms are actively employed in the ligand-field engineering of spin-flip luminescence transitions in molecular systems [39,58,90], which are direct molecular analogs to the spin-flip multiplets elaborated here. In this work, we show how the fundamental multiplet energies and their sequencing can be tuned by ligand-field engineering and the charge-transfer gap in the solid state. These underlying design principles could be fruitful for realizing deterministic optical properties in the field of vdW materials.

IV. CONCLUSIONS

In conclusion, we extensively investigated the properties of the sharp, spin-singlet multiplet excitations of the nickel dihalides (NiX_2) using RIXS. We demonstrated that nearly-resolution-limited *dd* excitations are ubiquitous features of octahedrally coordinated Ni^{2+}, which can be systematically tuned by the ligand and charge-transfer gap. We further established the roles of charge transfer states and magnetism, ruling out a Zhang-Rice mechanism and revealing that the fundamental multiplet peaks are independent of long-range magnetic order. Most importantly, we provided direct experimental evidence demonstrating that these excitations are dispersive. We connected this behavior with an emergent effect of the increased self-doped ligand-hole character of these excitations upon reduction of the charge-transfer gap. Finally, we identified a potential mechanism for this exciton delocalization that is mediated by the ligand states in analogy to superexchange. Our RIXS results thus firmly establish the microscopic nature of these exciton states, and provide a fundamentally distinct approach for tailoring collective electronic excitations in charge-transfer insulators through their momentum dispersion.

Note added. We note that a similar study has been performed in $NiPS_3$ [91]. The results for the $^1A_{1g}$ exciton energy scale (e.g., intra-atomic Hund's exchange) and the dispersion are compatible with the results presented here, highlighting the generality of our conclusions.

ACKNOWLEDGMENTS

We acknowledge insightful discussions with Maurits Haverkort, Ru-Pan Wang, and Krzysztof Wohlfeld. This work was supported by the U.S. Department of Energy, Office of Science National Quantum Information Science Research Center's Co-design Center for Quantum Advantage (C2QA), who led in this research, under Contract No. DE-SC0012704 (x-ray spectroscopy measurements and data analysis) and by the U.S. Department of Energy, BES under Award No. DE-SC0019126 (sample synthesis and characterization). This work was supported by the Laboratory Directed Research and Development project of Brookhaven National Laboratory No. 21-037. This research used beamline 2-ID of the National Synchrotron Light Source II, a U.S. Department of Energy (DOE), Office of Science User Facility operated for the DOE Office of Science by Brookhaven National Laboratory under Contract No. DE-SC0012704. This work was supported by the U.S. Department of Energy Office of Science, Early Career Research Program.

APPENDIX A: METHODS

1. Sample growth and preparation

All samples were prepared using chemical vapor transport. $NiCl_2$ was synthesized using stoichiometric ratios of nickel powder (Sigma-Aldrich, 99.9%) and $TeCl_4$ (Sigma-Aldrich, 99.8%), at a temperature gradient of 760 to 730 °C for 72 h before being cooled naturally to ambient conditions. The temperature ramp-up time was 72 h. Single-crystal $NiBr_2$ was grown from $NiBr_2$ powder (anhydrous, >99.9%, Sigma-Aldrich), at a temperature gradient 650 to 600 °C. Single-crystal NiI_2 was grown from elemental precursors with molar ratio $Ni:I = 1:2$, at a temperature gradient 700 to 500 °C as described previously [33]. The magnetic susceptibility was measured using a magnetic property measurement system (MPMS 3, Quantum Design Inc.) for $NiI_2/NiBr_2$ and a physical property measurement system (PPMS, Quantum Design Inc.) using the vibrating sample magnetometer option for $NiCl_2$. The magnetic susceptibility of the bulk crystals confirmed the magnetic transitions at $T_N = 53$ K for $NiCl_2$, $T_{N,1} = 45$ K and $T_{N,2} = 22$ K for $NiBr_2$, and $T_{N,1} = 75$ K and $T_{N,2} = 60$ K for NiI_2. Magnetic susceptibility data are shown in the Supplemental Material [47] for $NiCl_2$ and $NiBr_2$ and in Ref. [33] for the NiI_2.

The samples were aligned using a Bruker-GAADS Co-K_α ($\lambda = 1.7902$ Å) x-ray diffractometer to place the $\mathbf{a}^*$ direction in the scattering plane for RIXS experiments. The lattice parameters were determined to be $a = 3.465(12)$ Å and $c = 17.304(46)$ Å for $NiCl_2$, $a = 3.648(13)$ Å and $c = 18.412(52)$ Å for $NiBr_2$, and $a = 3.934(15)$ Å and $c = 19.809(61)$ Å for NiI_2, which were determined by single-crystal diffraction from the (006) and (104) reflections. Samples were aligned in air, cleaved in a high-purity nitrogen-filled glovebox (H_2O and $O_2 < 0.1$ ppm), and stored in vacuum for transport to the x-ray beamline. For NiI_2, we left the as-grown surface uncleaved for XRD alignment, with air exposure of approximately 15 min. Cleaving of the as-grown surface inside a nitrogen-filled glovebox after alignment revealed protected surfaces without degradation. The sharp multiplet features in agreement with optical spectra [15,17,29] and low diffuse scattering of the soft x-ray beam confirmed high-quality samples and flat vdW surfaces for all samples.

2. X-ray absorption and resonant inelastic x-ray scattering experiments

XAS and RIXS measurements at the Ni-L_3 edge (852 eV) were carried out at the 2-ID SIX beamline at the National Synchrotron Light Source II, Brookhaven National Laboratory. σ polarization was applied for the incident x rays for all measurements. XAS was recorded in TFY using a photodiode inside the soft x-ray chamber. RIXS spectra were recorded with high resolution of $\Delta E = 31$ meV for all measurements. The sample temperature was kept at 40 K unless specified. Laboratory-prepared and sealed samples were transferred from vacuum into the ultra-high-vacuum (UHV) loadlock of the x-ray chamber with minimal air exposure and kept under UHV conditions for the duration of the x-ray experiments. NiI_2 samples are more hygroscopic and were loaded into the vacuum chamber within a high-purity-nitrogen environment.

3. Charge-transfer multiplet calculations

We performed charge-transfer-multiplet (CTM) and crystal-field-multiplet (CFM) calculations using the QUANTY software [52–54]. For the CFM calculations, we considered the Ni-3d orbitals in the basis set with an octahedral crystal field (O_h, CF). For the CTM calculations, the symmetrized $X =$ Cl, Br, I molecular orbitals of t_{2g} and e_g symmetry were explicitly included. For the main text, we restricted all calculations to O_h symmetry, while the effects of the trigonal D_{3d} distortion are considered in the Supplemental Material [47]. Core-level spectra for the Ni-$L_{2/3}$ edges were calculated by considering $2p \to 3d$ dipole transitions using the Green's function formalism [52–54]. All spectra were calculated in the experimental polarization conditions.

The parameters for the multiplet calculations included the Coulomb interactions at the nickel site parametrized as the direct Slater integrals F^2_{dd} and F^4_{dd} in the initial and final RIXS states ($3d^8$) and by the direct integrals F^2_{dd}, F^4_{dd}, and F^2_{pd} and exchange integrals G^1_{pd} and G^3_{pd} in the intermediate RIXS state ($2p^5 3d^9$). The atomic spin-orbit coupling (SOC) in the $3d$ and $2p$ nickel states were also included. The Slater integrals and SOC parameters for each electronic configuration were taken from Hartree-Fock values tabulated by Haverkort [92], as shown in Table II. For the CTM calculations, all Slater integrals were uniformly scaled to atomic values [80% of Hartree-Fock (HF) values]. Additional parameters included the Coulomb repulsion parameters U_{dd} and $U_{pd} = 5.0$ and 7.0 eV, respectively (taken from photoemission experiments [23,24]), the charge-transfer energy Δ, and the metal-ligand hybridization $V(e_g)/V(t_{2g})$. We used the empirical relation $V(t_{2g}) = 3/5 \times V(e_g)$ and fit the XAS and RIXS spectra using $V(e_g)/\Delta$. The bare O_h-symmetry Ni-3d CF splitting ("ionic") was fixed to $10Dq = 0.55$ eV for all compounds. It was found that the best fit to each NiX_2 resulted in an approximately linear relation between Δ and $V(e_g)$ given by $V = 0.181 \times \Delta + 1.301$, which was used to generate Fig. 2(b). The overall parameters for the ligand dependence are summarized in Table I. The reported values are in good agreement with previous reports from XPS and XAS measurements [24], but are further restricted in our case by the RIXS data.

APPENDIX B: COMPARISON BETWEEN CTM AND CFM CALCULATIONS

Besides these CTM calculations, we also performed CFM calculations to investigate the role of the ligand-hole states. We fixed the O_h-symmetry crystal field to $10Dq = 0.95$ eV based on the lowest-energy $^3T_{2g}$ multiplet observed in all compounds. We then adjusted the direct Slater integral scaling F_k to find the optimum agreement with all other multiplet excitations in the RIXS spectra. Finally, we fixed F_k and varied the exchange integral scaling G_k, which contributes only in the intermediate-state Hamiltonian, to optimize the XAS profile, in particular the MP-SP splitting in the XAS. The optimized values for each compound are reported in Table III, which were used to calculate the effective nephelauxetic ratio reported in Table I.

We compared the calculated XAS and ground-state energy-level diagrams within the CTM and CFM frameworks in Fig. 6. From these comparisons, we concluded

TABLE II. Hartree-Fock parameters from Ref. [92] in the ground ($3d^8 2p^6$) and intermediate states ($3d^9 2p^5$) of Ni^{2+} used for all calculations. Units are in eV.

Configuration	F^2_{dd}	F^4_{dd}	ζ_{3d}	F^2_{pd}	G^1_{pd}	G^3_{pd}	ζ_{2p}
$3d^8 2p^6$	12.233	7.597	0.083	⋯	⋯	⋯	⋯
$3d^9 2p^5$	13.005	8.084	0.102	7.720	5.783	3.290	11.507

TABLE III. Ligand dependence of Coulomb screening parameters from optimized charge transfer multiplets calculations. The O_h crystal field is fixed to $10Dq = 0.95$ eV. Values are percent of Hartree-Fock values, where $F_k = G_k = 0.80$ correspond to atomic values. Uniform scaling of all parameters is used across the initial and intermediate states.

	F_k	G_k
$NiCl_2$	0.60	0.68
$NiBr_2$	0.51	0.51
NiI_2	0.35	0.22

that the evolution of the $^1A_{1g}$ and the ^1E_g peaks, as well as the MP-SP evolution, can be effectively mapped onto an ionic model and result from the intra-atomic Coulomb interactions at the nickel site. The near-resolution-limited behavior of these highlighted $^1A_{1g}$ and ^1E_g multiplets results from their low degeneracy: The $^1A_{1g}$ is both a spin and orbital singlet, while the ^1E_g is an orbital-doublet and spin-singlet state. As both of these spin-orbital excitations involve a rearrangement of the electronic configuration within the half-filled e_g crystal-field states, they are not sensitive to the crystal-field distortion, but are rather stabilized from the $^3A_{2g}$ ground state directly through the intra-atomic Hund's exchange interactions which are here parametrized by the Slater integrals $F^2_{dd} - F^4_{dd}$ in the initial state. This intraconfigurational excitation nature also results in a smaller coupling to phonons [15,19–21], which contributes to the qualitatively smaller linewidths compared to the other interconfigurational (e.g., $t^6_{2g}e^2_g \to t^5_{2g}e^3_g$) multiplets.

In the CFM model, the screening of the intra-atomic Coulomb interaction, or nephelauxetic effect, was accounted for by a direct reduction of the Slater integrals (e.g., $F_k - G_k$ scaling factors), while in the CTM calculations an effective reduction of the Coulomb interactions were induced by an enhanced self-doped ligand-hole ($3d^9\underline{L}$) character which naturally increased as the charge-transfer gap decreased [see Fig. 2(b)]. Thus, as electronic density is transferred to the surrounding ligands,

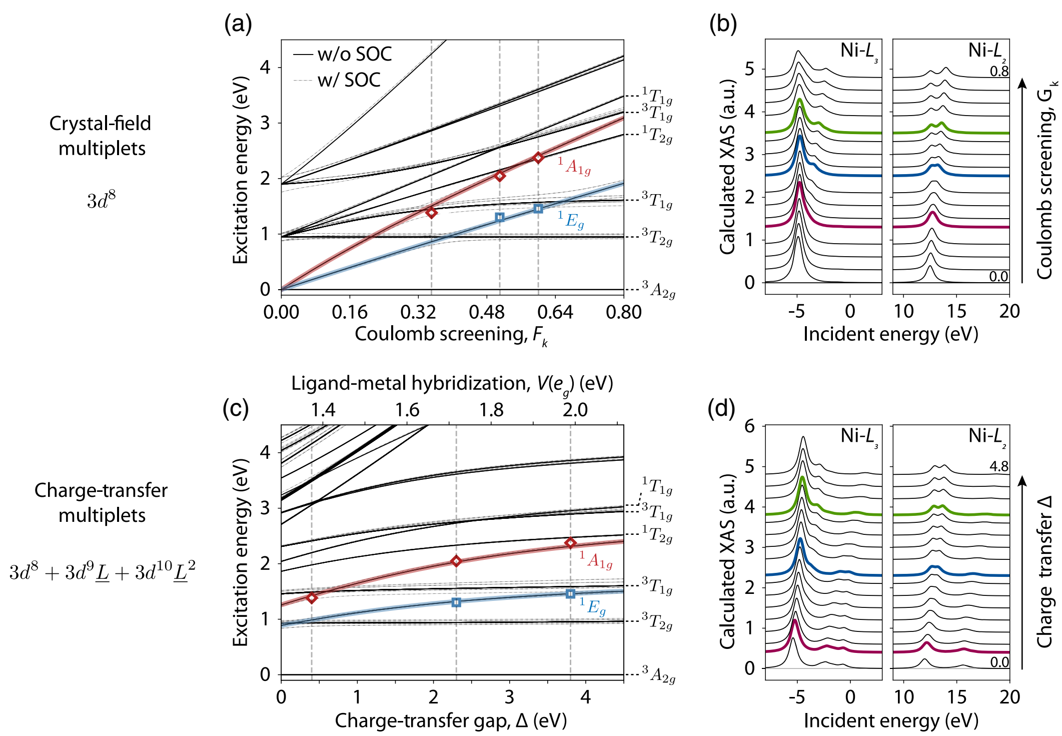

FIG. 6. Calculations of the multiplet structure within the crystal-field-multiplet (CFM) (top row) and CTM (bottom row) models. (a) $3d^8$ multiplet structure with $10Dq = 950$ meV as a function of the intra-atomic Coulomb screening F_k in the initial RIXS state, where $F_k = 0.80$ corresponds to atomic values. (b) The Ni-L_3 edge (left) and Ni-L_2 edge (right) simulated XAS spectra (offset vertically for clarity) as a function of the covaried direct (F_k) and exchange (G_k) Slater integrals in the initial and intermediate states. (c) Energy-level multiplet diagram in the charge-transfer model as a function of the covaried charge-transfer gap (Δ) and metal-ligand hybridization [$V(e_g)$] along with (d) the simulated XAS spectra. The covariant values $F_k - G_k$ and $\Delta - V(e_g)$ in the CFM and CTM models, respectively, are interpolated linearly between the best-fit values of the NiX_2 experimental data (see Tables III and I). In (a) and (c), thick red and blue lines highlight the $^1A_{1g}$ and ^1E_g excitations, respectively, and the experimentally observed excitation energies are shown as open red diamonds and blue squares, respectively, for $X =$ I, Br, Cl from left to right. The optimal parameter values are indicated by dashed vertical lines. In (b) and (d), the corresponding XAS spectra for these optimized values are reported in red, blue, and green for I, Br, and Cl, respectively.

the electronic interactions stabilizing the spin-singlet multiplets are reduced. Furthermore, the $^1A_{1g}$ and ^1E_g multiplet degeneracy is not sensitive to the inclusion of SOC, lowered (trigonal) CF symmetry, or effective spin-exchange field splitting, and they are not endowed with fine-structure broadening, leading to nearly resolution-limited behavior across the entire halide series, independent of the ligand-tuned covalency and charge-transfer state weight. We note that these conclusions are also consistent with previous observations in NiO [40].

While the essential physics can be accounted for only from a $3d^8$ model, the inclusion of charge-transfer states more accurately captures the excitation-dependent screening of the intra-atomic electronic interactions compared to a uniform screening introduced phenomenologically through the CFM model, resulting in an improvement in the description of the data. Additionally, higher-energy charge-transfer sidebands in the XAS and additional charge-transfer excitations in the RIXS spectra are captured in the CTM model, which are not included in the CFM approximation. In the CFM model, a separate tuning of the direct and exchange Coulomb interactions is required to describe the ligand-dependent screening in the initial and final (ground, $3d^8 2p^6$) and the intermediate (excited, $3d^9 2p^5$) states to accurately describe the $\Delta S = 1$ excitations in the RIXS spectrum and the L_3-edge XAS sideband evolution versus ligand. In contrast, the CTM model allows for a correct description of both features directly through tuning of the charge-transfer energy and the orbital-dependent hybridization. The source of these effects comes from larger hybridization of higher-energy excitations in both the initial and intermediate RIXS states with the charge-transfer states, leading to a larger effective screening of their Coulomb interactions. For this reason, the sideband multiplet in the intermediate $3d^9 2p^5$ state reflected in the XAS profile hybridizes more strongly at a given Δ than the main band multiplets, as depicted in Fig. 7, and similarly for the $^1A_{1g}$ excitation in the ground and final $3d^8$ state which occurs at higher energies relative to the $^3A_{2g}$ ground state compared to the ^1E_g excitation. This preferentially large hybridization may lead to the incorrect conclusion that the ligand states are essential to describe the physics of these excitations. However, larger ligand-hole state weight in these excitations is a consequence of the details of hybridization within this regime of the charge-transfer gap, and the dominant effect (as revealed directly through our comparison of ionic and charge-transfer calculations) is that hybridization with ligand states induces a nephelauxetic effect [25] which describes all salient features of the data, excluding the temperature and momentum dependence. This conclusion was directly proven by our ligand-dependent data and calculations and is in agreement with the known spectrochemical trends for halogen ligands [2,15,17,25,29,30,41].

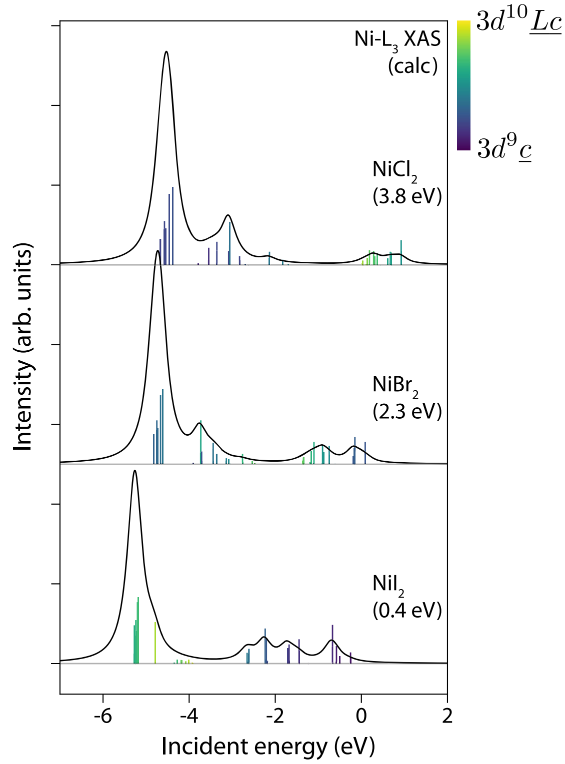

FIG. 7. Calculated Ni-L_3 edge XAS for optimized values in the CTM model for $NiCl_2$, $NiBr_2$, NiI_2 from top to bottom, respectively. The energy axis is with respect to the center energy of the $3d^9 2p^5$ configuration in the calculation. Individual excitations contributing to the XAS profile are shown as bar plots over the corresponding spectra, showing the evolution of each XAS transition between the $3d^9\underline{c}/3d^{10}\underline{L}\,\underline{c}$ ligand-hole character as Δ is reduced. The relative weight of each configuration is indicated by the color bar. See also the analogous plot for the ground-state multiplets in Fig. 2(b).

From the charge-transfer and crystal-field multiplet models, the XAS and RIXS core-level spectra at the Ni-L_2/L_3 edges were calculated with the Green's function approach as implemented in the software QUANTY [52–54]. We used a core-hole (Lorentzian) broadening of 500 meV for both XAS and RIXS spectra and a 30-meV Lorentzian broadening on the energy-transfer axis for the RIXS spectra. In addition, we introduced a mode-dependent broadening of specific excitations which did couple (interconfigurational, e.g., $^3T_{2g}$) and did not couple (intraconfigurational, e.g., $^1A_{1g} - {}^1E_g$) to the O_h crystal field by averaging several calculations calculated with different values of $10Dq$ with ± 50 meV of the best-fit value. This phenomenologically accounts for the distinct linewidths between these types of excitations related to a differential coupling to phonons which broaden the line shape of the $10Dq$-coupled excitations. Simulated RIXS maps for each compound in the CTM model are reported in Figs. 8(a)–8(c). These show good

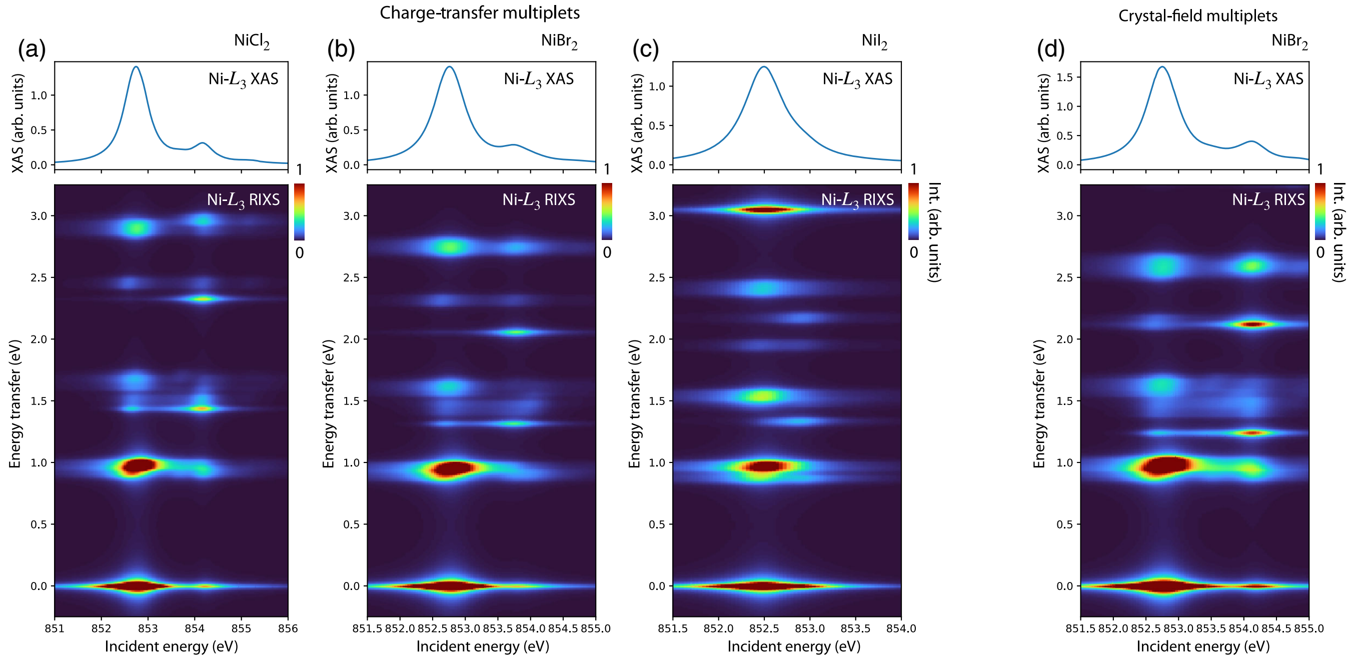

FIG. 8. Calculated incident-energy-dependent RIXS maps across the Ni-L_3 edge resonance alongside the calculated XAS in the CTM model for (a) $NiCl_2$, (b) $NiBr_2$, and (c) NiI_2, as well as the corresponding CFM result for $NiBr_2$ in (d). Parameters are described in the text. Spectra are calculated with Lorentzian broadening of 0.5 eV on the incident-energy axis (XAS and RIXS) and by 0.03 eV on the energy-transfer axis. In addition, an empirical, mode-dependent broadening is introduced by averaging spectra with different values of $10Dq$ in a range ± 0.05 eV around the central best value. Spectra are all calculated in the experimental polarization conditions.

agreement with the experimental data in Figs. 1(c)–1(e). We note in both the calculated and experimental RIXS maps an apparent shift of the $^3T_{2g}$ peak to higher energies in the XAS postedge region. This is attributed to intermediate-state cross-section effects which transfer spectral weight to different fine-structure components of the $^3T_{2g}$ state. Such a fine structure can be induced by the combined effects of spin-orbit coupling, effective spin exchange, and the trigonal distortion [51]. We also display a corresponding RIXS map calculation for the CFM model for optimized $NiBr_2$ parameters in Fig. 8(d). The CFM model RIXS map shows that the resonance of the spin-flip multiplets at the sideband is not related to the relative ligand-hole state character in the ground and intermediate states, but is dictated by a cross-section effect related to the $3d^8$ and $3d^9 2p^5$ ground- and intermediate-state multiplet structure and dipole-selection rules determined from Ni^{2+} in O_h symmetry. We note that this cross-section effect may be related to the $\Delta m_s = 2$ (two-magnon) excitations resonant at the sideband in NiO [40], which is attributed to the $2p$-$3d$ Coulomb exchange integral G^1_{pd}/G^3_{pd}. This is also consistent with our data on $NiCl_2$ and $NiBr_2$.

APPENDIX C: TEMPERATURE-DEPENDENCE DATA FOR THE ^1E_g AND $^1A_{1g}$ MULTIPLETS

The full temperature dependence of the ^1E_g and $^1A_{1g}$ multiplets for each compound is displayed in Fig. 9. These are the same measurements analyzed in Figs. 4(c)–4(f), where here we report the raw line cuts and fits for each compound. The measured data were taken at maximum momentum transfer (grazing-incidence geometry) along the ΓM momentum space cut, with σ incident polarization and with energy tuned to the respective SP resonance in the XAS, as reported in Fig. 1. The multiplets were fit with a single Gaussian peak to determine the full width at half maximum (FWHM) as a function of the temperature. Additional neighboring multiplets and additional spectral weight appearing as sidebands (particularly visible on the higher-energy-loss side of the $^1A_{1g}$ peak in $NiCl_2$ and $NiBr_2$, discussed below) were fit with additional Gaussian peaks in addition to a constant background. As in Figs. 4(d)–4(f), the gray dashed lines in the FWHM plots indicate linear fits. Error bars were determined from the standard error of the fits.

In the case of $NiCl_2$ and $NiBr_2$, the ^1E_g has an energy close to the $^3T_{1g}$ multiplet which appears at higher-energy loss in the displayed regions of Fig. 9, while the ^1E_g peak is not resolved in NiI_2. The additional spectral weight in the higher-energy-loss side of the $^1A_{1g}$ peaks in $NiCl_2$ and NiI_2 are associated with the $^1T_{2g}$ and $^3T_{1g}$ multiplets, respectively. These assignments are supported by our cluster calculations in Fig. 2 and the expanded discussion in Appendix B. Meanwhile, additional spectral weight appearing as a sideband at higher-energy loss of the $^1A_{1g}$

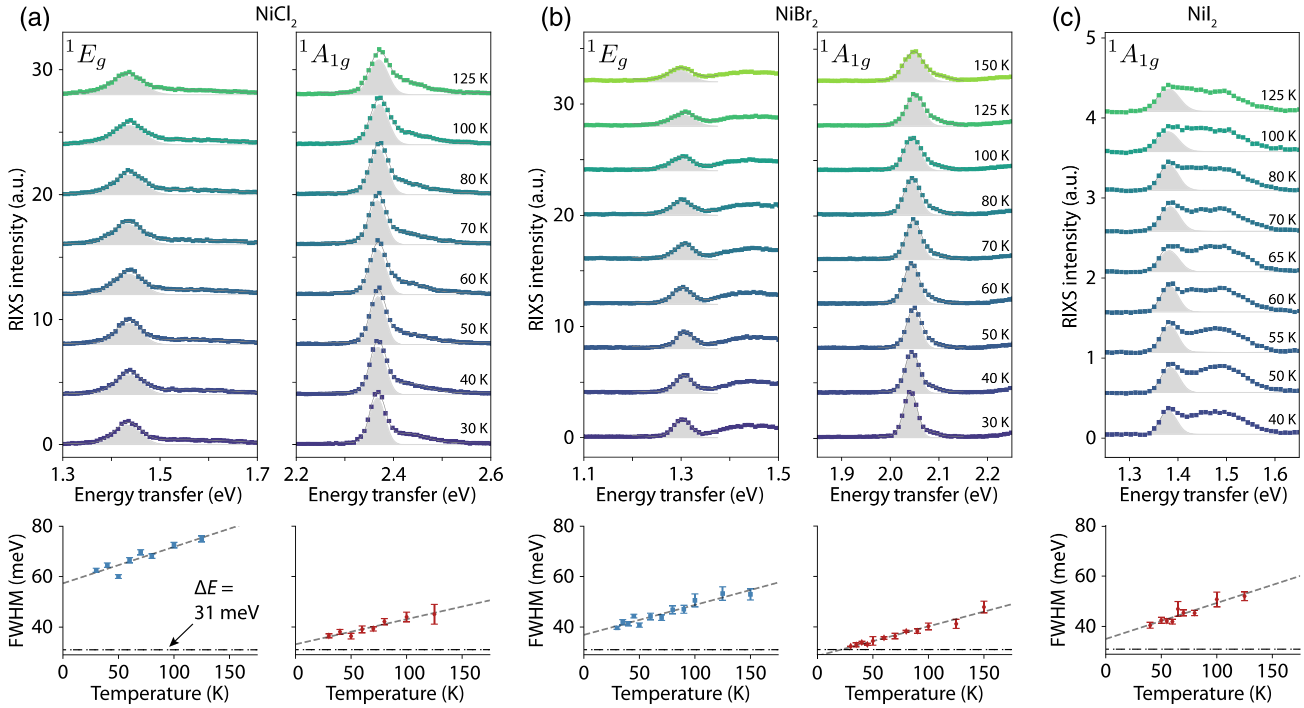

FIG. 9. Raw-temperature-dependent line cuts and fits for the ^1E_g and $^1A_{1g}$ multiplets in (a) $NiCl_2$, (b) $NiBr_2$, and (c) NiI_2. The FWHM of each peak as a function of the temperature, determined from Gaussian fits, is shown below each respective plot. The dashed line indicates the experimental resolution of $\Delta E = 31$ meV for all measurements. The spectra are all normalized by the counting time.

peak in $NiBr_2$ cannot be directly accounted for in the localized multiplet excitation spectrum. These are associated with two-phonon or magnon sidebands, consistent with their identification in optics experiments [15,18–21].

[1] R. S. Knox, *Introduction to exciton physics*, in *Collective Excitations in Solids* (Springer, New York, 1983), pp. 183–245.

[2] C. J. Ballhausen, *Introduction to Ligand Field Theory*, McGraw-Hill Series in Advanced Chemistry (McGraw-Hill, New York, 1962).

[3] V. M. Agranovich and B. S. Toshich, *Collective properties of Frenkel excitons*, Sov. Phys. JETP **26**, 104 (1968).

[4] Kyle L. Seyler, Ding Zhong, Dahlia R. Klein, Shiyuan Gao, Xiaoou Zhang, Bevin Huang, Efrén Navarro-Moratalla, Li Yang, David H. Cobden, Michael A. McGuire, Wang Yao, Di Xiao, Pablo Jarillo-Herrero, and Xiaodong Xu, *Ligand-field helical luminescence in a 2D ferromagnetic insulator*, Nat. Phys. **14**, 277 (2018).

[5] Zhaowei Zhang, Jingzhi Shang, Chongyun Jiang, Abdullah Rasmita, Weibo Gao, and Ting Yu, *Direct photoluminescence probing of ferromagnetism in monolayer two-dimensional* $CrBr_3$, Nano Lett. **19**, 3138 (2019).

[6] Suhan Son, Youjin Lee, Jae Ha Kim, Beom Hyun Kim, Chaebin Kim, Woongki Na, Hwiin Ju, Sudong Park, Abhishek Nag, Ke-jin Zhou, Young Woo Son, Hyeongdo Kim, Woo-suk Noh, Jae-hoon Park, Jong Seok Lee, Hyeonsik Cheong, Jae Hoon Kim, and Je-Geun Park, *Multiferroic-enabled magnetic-excitons in 2D quantum-entangled van der Waals antiferromagnet* NiI_2, Adv. Mater. **34**, 2109144 (2022).

[7] Soonmin Kang, Kangwon Kim, Beom Hyun Kim, Jonghyeon Kim, Kyung Ik Sim, Jae Ung Lee, Sungmin Lee, Kisoo Park, Seokhwan Yun, Taehun Kim, Abhishek Nag, Andrew Walters, Mirian Garcia-Fernandez, Jiemin Li, Laurent Chapon, Ke Jin Zhou, Young Woo Son, Jae Hoon Kim, Hyeonsik Cheong, and Je Geun Park, *Coherent many-body exciton in van der Waals antiferromagnet* $NiPS_3$, Nature (London) **583**, 785 (2020).

[8] Xingzhi Wang, Jun Cao, Zhengguang Lu, Arielle Cohen, Hikari Kitadai, Tianshu Li, Qishuo Tan, Matthew Wilson, Chun Hung Lui, Dmitry Smirnov, Sahar Sharifzadeh, and Xi Ling, *Spin-induced linear polarization of photoluminescence in antiferromagnetic van der Waals crystals*, Nat. Mater. **20**, 964 (2021).

[9] Dong Seob Kim, Di Huang, Chunhao Guo, Kejun Li, Dario Rocca, Frank Y. Gao, Jeongheon Choe, David Lujan, Ting-Hsuan Wu, Kung-Hsuan Lin, Edoardo Baldini, Li Yang, Shivani Sharma, Raju Kalaivanan, Raman Sankar, Shang-Fan Lee, Yuan Ping, and Xiaoqin Li, *Anisotropic excitons reveal local spin chain directions in a van der Waals antiferromagnet*, Adv. Mater. **35**, 2206585 (2023).

[10] Emre Ergeçen, Batyr Ilyas, Dan Mao, Hoi Chun Po, Mehmet Burak Yilmaz, Junghyun Kim, Je Geun Park, T. Senthil, and Nuh Gedik, *Magnetically brightened dark electron-phonon bound states in a van der Waals antiferromagnet*, Nat. Commun. **13**, 1 (2022).

[11] Dipankar Jana, P. Kapuscinski, I. Mohelsky, D. Vaclavkova, I. Breslavetz, M. Orlita, C. Faugeras, and M. Potemski, *Magnon gap excitations and spin-entangled optical transition in van der Waals antiferromagnet* $NiPS_3$, Phys. Rev. B **108**, 115149 (2023).

[12] Carina A. Belvin, Edoardo Baldini, Ilkem Ozge Ozel, Dan Mao, Hoi Chun Po, Clifford J. Allington, Suhan Son, Beom Hyun Kim, Jonghyeon Kim, Inho Hwang, Jae Hoon Kim, Je Geun Park, T. Senthil, and Nuh Gedik, *Exciton-driven antiferromagnetic metal in a correlated van der Waals insulator*, Nat. Commun. **12**, 4837 (2021).

[13] Dmytro Afanasiev, Jorrit R. Hortensius, Mattias Matthiesen, Samuel Mañas-Valero, Makars Šiškins, Martin Lee, Edouard Lesne, Herre S.J. van der Zant, Peter G. Steeneken, Boris A. Ivanov, Eugenio Coronado, and Andrea D. Caviglia, *Controlling the anisotropy of a van der Waals antiferromagnet with light*, Sci. Adv. **7**, 1 (2021).

[14] Peiyao Zhang, Ting-fung Chung, Quanwei Li, Siqi Wang, Qingjun Wang, Warren L. B. Huey, Sui Yang, Joshua E. Goldberger, Jie Yao, and Xiang Zhang, *All-optical switching of magnetization in atomically thin* CrI_3, Nat. Mater. **21**, 1373 (2022).

[15] M. Kozielski, I. Pollini, and G. Spinolo, *Electronic absorption spectra of* Ni^{2+} *in* $NiCl_2$ *and* $NiBr_2$. *(Phonon and magnon sidebands)*, J. Phys. C **5**, 1253 (1972).

[16] P. Day, A. Dinsdale, E. R. Krausz, and D. J. Robbins, *Optical and neutron diffraction study of the magnetic phase diagram of* $NiBr_2$, J. Phys. C **9**, 2481 (1976).

[17] C. Kuindersma, S. R. Boudewijm, and P. R. Haas, *Near-infrared d-d transitions of* NiI_2*,* $CdI_2:Ni^{2+}$*, and* CoI_2, Phys. Status Solidi (b) **108**, 187 (1981).

[18] D. J. Robbins and P. Day, *Temperature variation of exciton-magnon absorption bands in metamagnetic transition-metal dihalides*, J. Phys. C **9**, 867 (1976).

[19] I. Pollini, G. Spinolo, and G. Benedek, *Vibrational structure of crystal-field spectra in layered 3d-metal dihalides*, Phys. Rev. B **22**, 6369 (1980).

[20] P. Giordano, I. Pollini, L. Reatto, and G. Spinolo, ^1E_g *spin-forbidden transition in* $NiBr_2$*: Temperature dependence and magnetoabsorption*, Phys. Rev. B **17**, 257 (1978).

[21] G. Benedek, I. Pollini, L. Piseri, and R. Tubino, *Evidence of two-phonon vibronic progressions in layered 3d-metal dihalides*, Phys. Rev. B **20**, 4303 (1979).

[22] Xi Wang, Chengxin Xiao, Heonjoon Park, Jiayi Zhu, Chong Wang, Takashi Taniguchi, Kenji Watanabe, Jiaqiang Yan, Di Xiao, Daniel R. Gamelin, Wang Yao, and Xiaodong Xu, *Light-induced ferromagnetism in moiré superlattices*, Nature (London) **604**, 468 (2022).

[23] J. Zaanen, C. Westra, and G. A. Sawatzky, *Determination of the electronic structure of transition-metal compounds:* $2p$ *x-ray photoemission spectroscopy of nickel dihalides*, Phys. Rev. B **33**, 8060 (1986).

[24] G. van der Laan, J. Zaanen, G. A. Sawatzky, R. Karnatak, and J. M. Esteva, *Comparison of x-ray absorption with x-ray photoemission of nickel dihalides and* NiO, Phys. Rev. B **33**, 4253 (1986).

[25] Frank de Groot and Akio Kotani, *Core Level Spectroscopy of Solids* (CRC Press, Boca Raton, 2008), pp. 1–491.

[26] Daniel I. Khomskii, *Transition Metal Compounds* (Cambridge University Press, Cambridge, England, 2014), pp. 1–485.

[27] F. C. Zhang and T. M. Rice, *Effective Hamiltonian for the superconducting Cu oxides*, Phys. Rev. B **37**, 3759 (1988).

[28] L. H. Tjeng, B. Sinkovic, N. B. Brookes, J. B. Goedkoop, R. Hesper, E. Pellegrin, F. M. F. de Groot, S. Altieri, S. L. Hulbert, E. Shekel, and G. A. Sawatzky, *Spin-resolved photoemission on anti-ferromagnets: Direct observation of Zhang-Rice singlets in* CuO, Phys. Rev. Lett. **78**, 1126 (1997).

[29] E. J. K. B. Banda, *Optical absorption of* $NiPS_3$ *in the near-infrared, visible and near-ultraviolet regions*, J. Phys. C **19**, 7329 (1986).

[30] David R. Rosseinsky and Iain A. Dorrity, *Absorption spectrum of single crystals of* NiI_2 *at 300-5 K*, Inorg. Chem. **17**, 1600 (1978).

[31] P. A. Lindgard, R. J. Birgeneau, H. J. Guggenheim, and J. Als-Nielsen, *Spin-wave dispersion and sublattice magnetization in* $NiCl_2$, J. Phys. C **8**, 1059 (1975).

[32] L. P. Regnault, J. Rossat-Mignod, A. Adam, D. Billerey, and C. Terrier, *Inelastic neutron scattering investigation of the magnetic excitations in the helimagnetic state of* $NiBr_2$, J. Phys. (Paris) **43**, 1283 (1982).

[33] Qian Song, Connor A. Occhialini, Emre Ergeçen, Batyr Ilyas, Danila Amoroso, Paolo Barone, Jesse Kapeghian, Kenji Watanabe, Takashi Taniguchi, Antia S. Botana, Silvia Picozzi, Nuh Gedik, and Riccardo Comin, *Evidence for a single-layer van der Waals multiferroic*, Nature (London) **602**, 601 (2022).

[34] Throughout the paper, we use the terms exciton, multiplet, and *dd* excitation interchangeably. Such terminology is consistent with the usage of "Frenkel excitons" in reference to multiplet transitions in the early optical literature [3,15,17,18,29,35–37]. However, referring to these states as multiplet transitions avoids confusion with excitons of distinct microscopic origin (e.g., Wannier excitons) routinely observed in semiconductors.

[35] Smith Freeman, *Molecular-orbital theory of the excited-state exchange interaction*, Phys. Rev. B **7**, 3960 (1967).

[36] D. D. Sell, R. L. Greene, and Robert M. White, *Optical exciton-magnon absorption in* MnF_2, Phys. Rev. **158**, 489 (1967).

[37] S. Freeman and J. J. Hopfield, *Exciton-magnon interaction in magnetic insulators*, Phys. Rev. Lett. **21**, 910 (1968).

[38] L. L. Lohr, *Spin-forbidden electronic excitations in transition metal complexes*, Coord. Chem. Rev. **8**, 241 (1972).

[39] Winald Robert Kitzmann, Johannes Moll, and Katja Heinze, *Spin-flip luminescence*, Photochem. Photobiol. Sci. **21**, 1309 (2022).

[40] Abhishek Nag, H. C. Robarts, F. Wenzel, J. Li, Hebatalla Elnaggar, Ru Pan Wang, A. C. Walters, M. Garcia-Fernandez, F. M. F. de Groot, M. W. Haverkort, and Ke Jin Zhou, *Many-body physics of single and double spin-flip excitations in* NiO, Phys. Rev. Lett. **124**, 067202 (2020).

[41] M. G. Brik, S. J. Camardello, A. M. Srivastava, N. M. Avram, and A. Suchocki, *Spin-forbidden transitions in the spectra of transition metal iions and nephelauxetic effect*, ECS J. Solid State Sci. Technol. **5**, R3067 (2016).

[42] K. Okada, A. Kotani, and B. T. Thole, *Charge transfer satellites and multiplet splitting in x-ray photoemission spectra of late transition metal halides*, J. Electron Spectrosc. Relat. Phenom. **58**, 325 (1992).

[43] Joseph Dvorak, Ignace Jarrige, Valentina Bisogni, Scott Coburn, and William Leonhardt, *Towards 10 meV resolution: The design of an ultrahigh resolution soft x-ray RIXS spectrometer*, Rev. Sci. Instrum. **87**, 115109 (2016).

[44] F. M. F. de Groot, M. A. Arrio, P. Sainctavit, C. Cartier, and C. T. Chen, *Fluorescence yield detection: Why it does not measure the x-ray absorption cross section*, Solid State Commun. **92**, 991 (1994).

[45] R. Carboni, S. Giovannini, G. Antonioli, and F. Boscherini, *Self-absorption correction strategy for fluorescence-yield soft x-ray near edge spectra*, Phys. Scr. T **115**, 986 (2005).

[46] Ru Pan Wang, Hebatalla Elnaggar, Charles J. Titus, Keisuke Tomiyasu, Jaap Geessinck, Gertjan Koster, Federica Frati, Jun Okamoto, Di Jing Huang, and Frank M. F. de Groot, *Saturation and self-absorption effects in the angle-dependent 2p3d resonant inelastic x-ray scattering spectra of* Co^{3+}, J. Synchrotron Radiat. **27**, 979 (2020).

[47] See Supplemental Material at http://link.aps.org/supplemental/10.1103/PhysRevX.14.031007 for sample characterization, raw momentum-dependent RIXS data, details of fitting procedures, and an assessment of self-absorption and polarization cross-section effects.

[48] F. M. F. de Groot, J. C. Fuggle, B. T. Thole, and G. A. Sawatzky, *L_2, 3 x-ray-absorption edges of d^0 compounds:* K, Ca, Sc, *and* Ti *in O_h symmetry*, Phys. Rev. B **41**, 928 (1990).

[49] A. V. Ushakov, S. V. Streltsov, and D. I. Khomskii, *Crystal field splitting in correlated systems with negative charge-transfer gap*, J. Phys. Condens. Matter **23**, 445601 (2011).

[50] A. Scaramucci, J. Ammann, N. A. Spaldin, and C. Ederer, *Separating different contributions to the crystal-field parameters using Wannier functions*, J. Phys. Condens. Matter **27**, 175503 (2015).

[51] F. M. F. de Groot, P. Kuiper, and G. A. Sawatzky, *Local spin-flip spectral distribution obtained by resonant x-ray Raman scattering*, Phys. Rev. B **57**, 14584 (1998).

[52] M. W. Haverkort, G. Sangiovanni, P. Hansmann, A. Toschi, Y. Lu, and S. Macke, *Bands, resonances, edge singularities and excitons in core level spectroscopy investigated within the dynamical mean-field theory*, Europhys. Lett. **108**, 57004 (2014).

[53] M. W. Haverkort, M. Zwierzycki, and O. K. Andersen, *Multiplet ligand-field theory using Wannier orbitals*, Phys. Rev. B **85**, 165113 (2012).

[54] Y Lu, M Höppner, O Gunnarsson, and M. W. Haverkort, *Efficient real-frequency solver for dynamical mean-field theory*, Phys. Rev. B **90**, 085102 (2014).

[55] We note the distinction between these local spin-state excitations (e.g., $S = 1 \rightarrow S = 0$) and the single- or two-magnon excitations [40,62,63]. The former excitations, considered here, are *dd* excitations stabilized by Hund's exchange. The latter excitations are transitions of the spin projection $\Delta m_s = 1$ within the triplet ground state, with characteristic energies determined by the effective spin exchange [2,25,51].

[56] K. Takubo, T. Mizokawa, J. Y. Son, T. Nambu, S. Nakatsuji, and Y. Maeno, *Unusual superexchange pathways in an* NiS_2 *triangular lattice with negative charge-transfer energy*, Phys. Rev. Lett. **99**, 037203 (2007).

[57] Valentina Bisogni, Sara Catalano, Robert J. Green, Marta Gibert, Raoul Scherwitzl, Yaobo Huang, Vladimir N. Strocov, Pavlo Zubko, Shadi Balandeh, Jean Marc Triscone, George Sawatzky, and Thorsten Schmitt, *Ground-state oxygen holes and the metal-insulator transition in the negative charge-transfer rare-earth nickelates*, Nat. Commun. **7**, 13017 (2016).

[58] Michael K. Wojnar, Daniel W. Laorenza, Richard D. Schaller, and Danna E. Freedman, *Nickel(II) metal complexes as optically addressable qubit candidates*, J. Am. Chem. Soc. **142**, 14826 (2020).

[59] J. Schlappa, K. Wohlfeld, K. J. Zhou, M. Mourigal, M. W. Haverkort, V. N. Strocov, L. Hozoi, C. Monney, S. Nishimoto, S. Singh, A. Revcolevschi, J. S. Caux, L. Patthey, H. M. Rønnow, J. van den Brink, and T. Schmitt, *Spin-orbital separation in the quasi-one-dimensional Mott insulator* Sr_2CuO_3, Nature (London) **485**, 82 (2012).

[60] Valentina Bisogni, Krzysztof Wohlfeld, Satoshi Nishimoto, Claude Monney, Jan Trinckauf, Kejin Zhou, Roberto Kraus, Klaus Koepernik, Chinnathambi Sekar, Vladimir Strocov, Bernd Büchner, Thorsten Schmitt, Jeroen van den Brink, and Jochen Geck, *Orbital control of effective dimensionality: From spin-orbital fractionalization to confinement in the anisotropic ladder system* $CaCu_2O_3$, Phys. Rev. Lett. **114**, 096402 (2015).

[61] Leonardo Martinelli *et al.*, *Collective nature of orbital excitations in layered cuprates in the absence of apical oxygens*, Phys. Rev. Lett. **132**, 066004 (2024).

[62] Jiemin Li, Yanhong Gu, Yoshihiro Takahashi, Keisuke Higashi, Taehun Kim, Yang Cheng, Fengyuan Yang, Jan Kunes, Jonathan Pelliciari, Atsushi Hariki, and Valentina Bisogni, *Single- and multimagnon dynamics in antiferromagnetic* α-Fe_2O_3 *thin films*, Phys. Rev. X **13**, 011012 (2023).

[63] Hebatalla Elnaggar, Abhishek Nag, Maurits W. Haverkort, Mirian Garcia-Fernandez, Andrew Walters, Ru Pan Wang, Ke Jin Zhou, and Frank de Groot, *Magnetic excitations beyond the single- and double-magnons*, Nat. Commun. **14**, 2749 (2023).

[64] S. R. Kuindersma, J. P. Sanchez, and C. Haas, *Magnetic and structural investigations on* NiI_2 *and* CoI_2, Physica (Amsterdam) **111B**, 231 (1981).

[65] Pierluigi Cudazzo, Francesco Sottile, Angel Rubio, and Matteo Gatti, *Exciton dispersion in molecular solids*, J. Phys. Condens. Matter **27**, 113204 (2015).

[66] Sonja Gombar, Petar Mali, Milan Pantić, Milica Pavkov-Hrvojević, and Slobodan Radošević, *Dynamics of Frenkel excitons in pentacene*, Materials **11**, 2219 (2018).

[67] A. Nag, A. Nocera, S. Agrestini, M. Garcia-Fernandez, A. C. Walters, Sang Wook Cheong, S. Johnston, and Ke Jin Zhou, *Quadrupolar magnetic excitations in an isotropic spin-1 antiferromagnet*, Nat. Commun. **13**, 1 (2022).

[68] L. Braicovich, L. J. P. Ament, V. Bisogni, F. Forte, C. Aruta, G. Balestrino, N. B. Brookes, G. M. De Luca, P. G. Medaglia, F. Miletto Granozio, M. Radovic, M. Salluzzo, J. van den Brink, and G. Ghiringhelli, *Dispersion of magnetic excitations in the cuprate* La_2CuO_4 *and* $CaCuO_2$ *compounds measured using resonant x-ray scattering*, Phys. Rev. Lett. **102**, 167401 (2009).

[69] L. Braicovich, J. van den Brink, V. Bisogni, M. M. Sala, L. J. P. Ament, N. B. Brookes, G. M. De Luca, M. Salluzzo, T. Schmitt, V. N. Strocov, and G. Ghiringhelli, *Magnetic excitations and phase separation in the underdoped* $La_{2-x}Sr_xCuO_4$ *superconductor measured by resonant inelastic x-ray scattering*, Phys. Rev. Lett. **104**, 077002 (2010).

[70] J. J. Lee, B. Moritz, W. S. Lee, M. Yi, C. J. Jia, A. P. Sorini, K. Kudo, Y. Koike, K. J. Zhou, C. Monney, V. Strocov, L. Patthey, T. Schmitt, T. P. Devereaux, and Z. X. Shen, *Charge-orbital-lattice coupling effects in the dd excitation profile of one-dimensional cuprates*, Phys. Rev. B **89**, 041104(R) (2014).

[71] Danila Amoroso, Paolo Barone, and Silvia Picozzi, *Spontaneous skyrmionic lattice from anisotropic symmetric exchange in a Ni-halide monolayer*, Nat. Commun. **11**, 5784 (2020).

[72] A. S. Botana and M. R. Norman, *Electronic structure and magnetism of transition metal dihalides: Bulk to monolayer*, Phys. Rev. Mater. **3**, 044001 (2019).

[73] E. Rastelli, A. Tassi, and L. Reatto, *Non-simple magnetic order for simple Hamiltonians*, Physica (Amsterdam) **97B+C**, 1 (1979).

[74] R. Fumagalli, J. Heverhagen, D. Betto, R. Arpaia, M. Rossi, D. Di Castro, N. B. Brookes, M. Moretti Sala, M. Daghofer, L. Braicovich, K. Wohlfeld, and G. Ghiringhelli, *Mobile orbitons in* Ca_2CuO_3*: Crucial role of Hund's exchange*, Phys. Rev. B **101**, 205117 (2020).

[75] J. Kim, D. Casa, M. H. Upton, T. Gog, Y. J. Kim, J. F. Mitchell, M. van Veenendaal, M. Daghofer, J. van den Brink, G. Khaliullin, and B. J. Kim, *Magnetic excitation spectra of* Sr_2IrO_4 *probed by resonant inelastic x-ray scattering: Establishing links to cuprate superconductors*, Phys. Rev. Lett. **108**, 177003 (2012).

[76] Jungho Kim, M. Daghofer, A. H. Said, T. Gog, J. van den Brink, G. Khaliullin, and B. J. Kim, *Excitonic quasiparticles in a spin-orbit Mott insulator*, Nat. Commun. **5**, 1 (2014).

[77] M. Kusch, V. M. Katukuri, N. A. Bogdanov, B. Büchner, T. Dey, D. V. Efremov, J. E. Hamann-Borrero, B. H. Kim, M. Krisch, A. Maljuk, M. M. Sala, S. Wurmehl, G. Aslan-Cansever, M. Sturza, L. Hozoi, J. van den Brink, and J. Geck, *Observation of heavy spin-orbit excitons propagating in a nonmagnetic background: The case of* $(Ba,Sr)_2YIrO_6$, Phys. Rev. B **97**, 064421 (2018).

[78] Ru Pan Wang, Atsushi Hariki, Andrii Sotnikov, Federica Frati, Jun Okamoto, Hsiao Yu Huang, Amol Singh, Di Jing Huang, Keisuke Tomiyasu, Chao Hung Du, Jan Kuneš, and Frank M. F. de Groot, *Excitonic dispersion of the intermediate spin state in* $LaCoO_3$ *revealed by resonant inelastic x-ray scattering*, Phys. Rev. B **98**, 035149 (2018).

[79] Peter Abbamonte, Tim Graber, James P. Reed, Serban Smadici Chen-lin Yeh, Abhay Shukla, Jean-pascal Rueff, and Wei Ku, *Dynamical reconstruction of the exciton in* LiF *with inelastic x-ray scattering*, Proc. Natl. Acad. Sci. U.S.A. **105**, 12159 (2008).

[80] Pierluigi Cudazzo, Matteo Gatti, Angel Rubio, and Francesco Sottile, *Frenkel versus charge-transfer exciton dispersion in molecular crystals*, Phys. Rev. B **88**, 195152 (2013).

[81] R. Schuster, M. Knupfer, and H. Berger, *Exciton band structure of pentacene molecular solids: Breakdown of the Frenkel exciton model*, Phys. Rev. Lett. **98**, 037402 (2007).

[82] K. Yang, L. P. Chen, Y. Q. Cai, N Hiraoka, S. Li, J. F. Zhao, D. W. Shen, H. F. Song, H. Tian, L. H. Bai, Z. H. Chen, Z. G. Shuai, and D. L. Feng, *Inelastic x-ray scattering study of exciton properties in an organic molecular crystal*, Phys. Rev. Lett. **98**, 036404 (2007).

[83] Richard S. Meltzer, Marian Lowe, and Donald S. McClure, *Magnon sidebands in the optical absorption spectrum of* MnF_2, Phys. Rev. **180**, 561 (1969).

[84] A. Pogrebna, S. Barsaume, R. R. Subkhangulov, A. V. Telegin, Y. P. Sukhorukov, A. V. Chzhan, T. Rasing, and A. V. Kimel, *Spectral tunability of laser-induced spin dynamics in the ferromagnetic semiconductor* $CdCr_2Se_4$, Phys. Rev. B **98**, 214427 (2018).

[85] G. M. Genkin, Y. N. Nozdrin, I. D. Tokman, and V. N. Shastin, *Direct observation of photomagnetization of the ferromagnet* $CdCr_2Se_4$ *by circularly polarized light*, JETP Lett. **35**, 199 (1982).

[86] Youn Jue Bae, Jue Wang, Allen Scheie, Junwen Xu, Daniel G. Chica, Geoffrey M. Diederich, John Cenker, Michael E. Ziebel, Yusong Bai, Haowen Ren, Cory R. Dean, Milan Delor, Xiaodong Xu, Xavier Roy, Andrew D. Kent, and Xiaoyang Zhu, *Exciton-coupled coherent magnons in a 2D semiconductor*, Nature (London) **609**, 282 (2022).

[87] Mattias Matthiesen, J. R. Hortensius, Samuel Manas-Valero, Itzik Kapon, Dumitru Dumcenco, Enrico Giannini, Makars Siskins, B. A. Ivanov, H. S. J. van der Zant, Eugenio Coronado, A. B. Kuzmenko, Dmytro Afanasiev, and A. D. Caviglia, *Controlling magnetism with light in a zero orbital angular momentum antiferromagnet*, Phys. Rev. Lett. **130**, 076702 (2023).

[88] Kyle Hwangbo, Qi Zhang, Qianni Jiang, Yong Wang, Jordan Fonseca, Chong Wang, Geoffrey M. Diederich, Daniel R. Gamelin, Di Xiao, Jiun Haw Chu, Wang Yao, and Xiaodong Xu, *Highly anisotropic excitons and multiple phonon bound states in a van der Waals antiferromagnetic insulator*, Nat. Nanotechnol. **16**, 655 (2021).

[89] Meng Wu, Zhenglu Li, Ting Cao, and Steven G. Louie, *Physical origin of giant excitonic and magneto-optical responses in two-dimensional ferromagnetic insulators*, Nat. Commun. **10**, 2371 (2019).

[90] S. L. Bayliss, D. W. Laorenza, P. J. Mintun, B. D. Kovos, D. E. Freedman, and D. D. Awschalom, *Optically addressable molecular spins for quantum information processing*, Science **370**, 1309 (2020).

[91] W. He, Y. Shen, K. Wohlfeld, J. Sears, J. Li, J. Pelliciari, M. Walicki, S. Johnston, E. Baldini, V. Bisogni, M. Mitrano, and M. P. M. Dean, *Magnetically propagating Hund's exciton in van der Waals antiferromagnet* $NiPS_3$, Nat. Commun. **15**, 3496 (2024).

[92] M. W. Haverkort, *Spin and orbital degrees of freedom in transition metal oxides and oxide thin films studied by soft x-ray absorption spectroscopy*, arXiv:cond-mat/0505214.

Correction: Missing information in the Acknowledgments section has been inserted.